DC Reluctance Machine – A Doubly-Salient Reluctance Machine with Controlled Electrical and Mechanical Power Ripple

Ethan Baggett Swint

Dissertation submitted to the faculty of the Virginia Polytechnic Institute and State University in partial fulfillment of the requirements for the degree of

Doctor of Philosophy
In
Electrical Engineering

Jih-Sheng Lai
Wensong Yu
Daniel Stilwell
Hardus Odendaal
Doug Nelson

27 February 2012
Blacksburg, VA

Keywords: Shaped Reluctance Machine, DC Reluctance Machine, Doubly-Salient Reluctance Machine, Switched Reluctance Machine, Torque Ripple, Current Ripple, Power Ripple

DC Reluctance Machine – A Doubly-Salient Reluctance Machine with Controlled Electrical and Mechanical Power Ripple

Ethan Baggett Swint

ABSTRACT

Doubly-Salient Reluctance Machines (DSRMs) sidestep many of the issues with permanent magnet and induction machines and embody the lowest cost and simplest manufacturing of the motor technologies. Major drawbacks to RMs have been (1) the need for failure-prone electrolytic capacitors, (2) large torque ripple, and (3) acoustic noise. Conventionally, these drawbacks have been addressed independently either through (1) excitation control or (2) machine design, but not as a holistic system or solution. This disseratation presents a design for high-efficiency low-cost RM while producing smooth output torque and avoiding pulsating inverter input current and the associated electrolytic capacitor. We propose a method for shaping the machine reluctance profile to reduce machine torque ripple to a desired level (here, <5%) without compromising on machine efficiency or power density, a Shaped Reluctance Machine (ShRM). Furthermore, a comprehensive approach which combines both phase excitation control and machine design to cooperatively address the excursions of input and output powers from their average values which results in less than 5% ripple for both electrical and mechanical net power – essentially a DC Reluctance Machine (DCRM). Compared to conventional practice in DSRMs, electrical power ripple is reduced by 85 times and torque ripple is reduced by almost 20 times, while overall efficiency, torque density, and power density are maintained.

Dedication

This work is dedicated to my wife, Pamela, who stuck with it at times when I was ready to fold, to my daughter, Lily, who's constant nagging helped propel me to finish ('How's the robot motor?', 'Is it moving?', 'How's the robot motor story?', 'Did you get your piece of paper?'), and my son, Malcolm, who won't remember what the fuss was all about. And to my parents, Dr. Richard and Susan Swint, who always established high expectations and gave me the means and tools to achieve them.

Acknowledgment

This work would not have been possible without Dr. Jih-Sheng Lai, whose generous and gracious support brought it back from the brink of abandonment. Dr. Richard Wallace, of the Whirlpool Corporation, whose technical (static torque curves) and emotional support moved the project along. Seung-Ryul Moon obtained the static inductance measurements and is prepped to advance the work in the lab. Also, the members of my advisory committee: Drs. Wen-song Yu, Daniel Stilwell, Hardus Odendaal, and Douglas Nelson, whose input and criticisms were greatly appreciated and made for a better dissertation.

My journey was enabled by the generous grant of Bradley Fellowship by the Via family in honor of Harry Lynde Bradley. This award gave the freedom to pursue my interests and was critical to the pursuit of my goals.

Table of Contents

Chapter 1: Introduction.....1

1.1 RM Fundamentals.....4

1.2 Idealized RM.....8

1.3 Power Ripple in RMs.....10

1.3.1 Mechanical Power Ripple: Origins and Solutions.....10

1.3.2 Electrical Power Ripple: Origins and Solutions.....19

1.3.3 Combined Power Ripple: Solutions.....25

1.4 Summary.....26

Chapter 2: Reluctance Shaping.....27

2.1 Geometric parametrization.....28

2.2 Perturbation process.....31

2.2.1 Gap perturbation 31

2.2.2 Identification of torque perturbation 32

2.2.3 Gap-torque perturbation map.....37

2.3 Design study in FEA 41

2.4 Summary.....45

Chapter 3: Excitation Shaping.....48

Chapter 4: DC Reluctance Machine Design.....52

4.1 Selection of Perturbation Mode.....53

4.2 Target Machine Specifications.....54

4.3 Design Refinement Process with FEA.....56

4.4 Comparison to Conventional SRM.....59

4.5 Summary.....60

Chapter 5: Experimental Results.....61

5.1 Static Tests.....62

5.2 Dynamic Tests.....66

Chapter 6: Conclusions.....76

6.1 Summary.....76

6.2 Contributions.....78

6.3 Future Work.....79

6.4 Conclusion.....81

6.5 Publications.....82

References.....83

List of Figures

Fig. 1.1: The simplicity of construction is evident in the DSRM.....2

Fig. 1.2: Typical silicon steel BH curve [4].....5

Fig. 1.3: Idealized DSRM allows simple phase excitation strategy.....8

Fig. 1.4: Idealized DSRM produces constant torque with excitation from Fig. 1.11.....9

Fig. 1.5: Typical SRM torque ripple from FEA for three machines with the same average torque output.....11

Fig. 1.6: Varied rotor pole widths [15].....12

Fig. 1.7: Wedge-shaped stator pole [17]. 12

Fig. 1.8: Rectangular void at leading edge and addition at trailing edge [22].....13

Fig. 1.9: Rectangular cutout on rotor pole [23].....14

Fig. 1.10: Three pole profiles: tapered, sawtoooth, and chamfered. [12].....14

Fig. 1.11: Notch on pole side and linear r vs theta on face. [25].....14

Fig. 1.12: Pole face from non-concentric arc. [26].....15

Fig. 1.13: Continuous first derivative in rotor surface [27].....15

Fig. 1.14: Notch on side of rotor pole. [25].....16

Fig. 1.15: Interior void on rotor. [29].....16

Fig. 1.16: Net electrical power (green) sees a large peak-to-peak ripple and discontinuity under conventional excitation.....19

Fig. 1.17: A blocking diode in the drive prevents negative supply current [63].....21

Fig. 1.18: The control method described in [62] adds long tail currents to the outgoing phase (top), largely avoiding negative current from the course (bottom).....22

Fig. 1.19: LC-filtered source input in [64].....23

Fig. 1.20: Simulated wave forms at 30% of rated power in [64].....24

Fig. 2.1: The original and modified gap function, due to a Gaussian perturbation.....32

Fig. 2.2: The original, modified and perturbation of the phase torque due to a Gaussian perturbation of the gap function, g.`.....33

Fig. 2.3: The torque perturbation and its Gaussian estimate.....36

Fig. 2.4: Map between Gaussian centers.....38

Fig. 2.5: Map between Gaussian magnitudes.....39

Fig. 2.6: Map between Gaussian widths.....40

Fig. 2.7: Torque error and its Gaussian model.....42

Fig. 2.8: Evolution of machine during refinement, clockwise from top left: gap function, torque, core loss, phase power, and phase current.....44

Fig. 3.1: The effects of perturbation of excitation voltage on other machine waveforms.....51

Fig. 4.1: Lamination design for 3-phase, 12/16 machine.....55

Fig. 4.2: Initial electrical (top) and mechanical (bottom) power wave forms for a conventional three-phase SRM.....57

Fig. 4.3: Final electrical (left) and mechanical (right) power wave forms for a three-phase DCRM.....57

Fig. 4.4: Air gap of DCR, in relation to that of the ShRM in Chapter 3.....58

Fig. 5.1: The prototype machine.....62

Fig. 5.2: Experimental vs modeled static torque waveforms at various currents.....63

Fig. 5.3: Phase inductance measurements for the prototype machine.....64

Fig. 5.4: Using the final current profile from the FEA refinement process (left), the per-phase and net torque (right) are calculated based on the static torque waveforms 65
Fig. 5.5: Dynamometer setup for dynamic testing of prototype DCRM.....67
Fig. 5.6: The DCRM is driven by a conventional asymmetric half-bridge converter and connected to the DC voltage source through an LC low-pass filter.....67
Fig. 5.7: Block diagram of DCRM controller.....68
Fig. 5.8: Raw experimental waveforms for 3 load points.....69
Fig. 5.9: Isolation of the phase frequency harmonics.....69
Fig. 5.10: Filtered experimental waveforms for 3 load points.....71
Fig. 5.11: Machine efficiency at various load points.....73

List of Tables

Table I FEA Refinement of Torque Ripple.....45

Table II Torque Ripple, Rotor Perturbation, and Resultant Torque Perturbation.....46

Table III FEA Refinement of Torque Ripple.....47

Table IV Key Machine Parameters.....55

Table V FEA Refinement of Power Ripple.....58

Table VI SRM and DCRM Comparison.....59

Table VII Power Ripple, Experimental Tests.....72

Table VIII Experimental Test Measurements, Part I.....74

Table IX Experimental Test Measurements, Part II.....75

Chapter 1: Introduction

The object of this investigation is to develop a design algorithm for Reluctance Machines (RMs) so that ripple in the electrical and mechanical power in the drive system can be reduced or eliminated, creating a DC Reluctance Machine (DCRM). Doubly Salient Reluctance Machines (DSRMs) are the simplest motor technology in terms of the number of materials and assembly, thereby holding the potential to be the least expensive and most robust. They consist of one or more fixed and one or more nonstationary magnetic cores with a salience in the reluctance path that is dependent upon the relative position of the fixed and movable cores. The nonstationary cores could be allowed to translate (linear machine) or rotate (rotary machine). For this work, discussion will be limited to the rotary machines, but throughout the terms "rotor" can be replaced with "translator" and angular quantities can be transformed into linear.

The salience of rotor and stator are accomplished through the placement of teeth on both cores. The magnetic circuit is energized by a conductor coil concentrated about one tooth on the stator. Neither conductors are needed on the rotor nor are any other sources of magnetization, such as permanent magnets, so the construction of reluctance machines avoids the need for complex fabrication techniques, such as the cast aluminum bars of induction machines or the procurement and installation of permanent magnets in brushless dc machines. A recently developed example of DSRM construction is shown in Fig. 1.1.

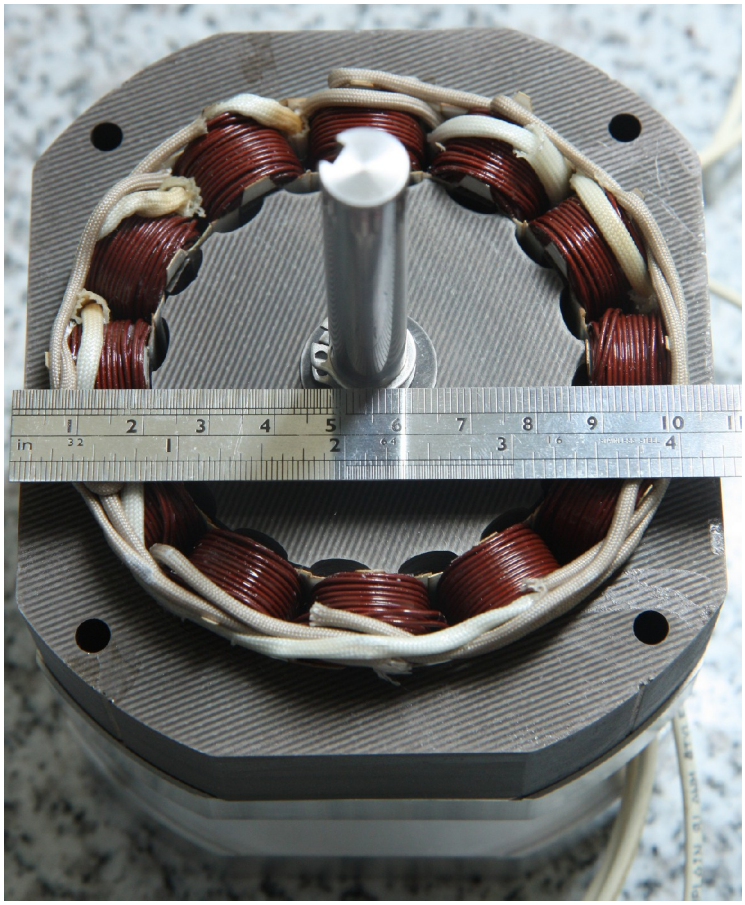

Fig. 1.1: The simplicity of construction is evident in the DSRM.

The most common reference to these types of machines at present is the Switched Reluctance Machine, or SRM, due to the switching on or off of the voltages applied to the phase windings. A similar term was used as the title of [1], "D.C.-switched Reluctance Machine," and "electronically-switched reluctance machine" was used in [2] to describe the adoption of new power electronic devices to control electrical power in the system. Prior to [2], one term that was employed was vernier reluctance machine [3], as an unequal number of rotor and stator poles are chosen such that only a fraction of the poles are aligned. The pole numbers dictate how many

independently controlled electrical phases there are in the machine and how many electrical cycles are completed in one mechanical revolution.

The simplicity in construction of DSRMs, however, belies the complexity in the design and control of the machine. Due to the difficulty in addressing this complexity, the electric and mechanical powers in RMs are subject to large ripples. In the electrical sense, this is exhibited by a large ripple in the net current flowing through the machines; in the mechanical, a large torque ripple is present. The rest of this chapter is devoted to an exposition to the problems affecting DSRMs and their causes, then to their treatment in contemporary literature.

Chapter 2 is devoted to the reduction of torque ripple, or mechanical power ripple. Chapter 3 provides an algorithm for reduction of ripple in the system's input current and electrical power. Chapter 4 combines these approaches to produce a DCRM through simulation in Finite Element Analysis. Chapter 5 provides experimental results of a physical system based on the design presented in the previous chapter. Finally, Chapter 6 concludes the work and summarizes the accomplishments and future work.

1.1 RM Fundamentals

In this section, we provide some of the basic definitions and equations relating the machine's geometry and electrical characteristics to the dynamic behavior of the machine. As the main subject of this work is "reluctance machines," we provide the definition of magnetic reluctance as

$$\Re = \frac{N i}{\varphi} \tag{1.1}$$

which is the ratio of the magneto-motive force (mmf) in ampere-turns, *Ni*, to the magnetic flux passing through a surface, Φ. By employing Ampere's law, the mmf can be expressed as

$$N i = \oint \bar{H} \cdot d\bar{l}_A \tag{1.2}$$

where $\bar{l}_A$ describes an amperian loop through the magnetic circuit and $\bar{H}$ is the magnetization. The magnetic flux is defined as

$$\varphi = \int \bar{B} \cdot d\bar{A} \tag{1.3}$$

where $\bar{B}$ is the magnetic field and $\bar{A}$ is the surface through which the field is flowing. Thus, reluctance can be expressed as

$$\Re = \frac{\oint H \cdot d\bar{l}}{\int \bar{B} \cdot d\bar{A}} \tag{1.4}$$

and lends itself to the interpretation of an aspect ratio: the length of the path over the cross-sectional area of the conduction medium. This is similar to the electrical resistance,

$$R = \rho \frac{l}{A}, \tag{1.5}$$

which gives rise to the notion of a magnetic equivalent circuit.

Electrical machines are predominately constructed of air, with a relative magnetic permeability of one, and some type of soft ferromagnetic material, such as silicon steel. A typical silicon steel *BH* curve is represented in Fig. 1.2 [4], which has a relative permeability in the range of 1000 at low levels of induction, but the permeability decreases significantly at higher levels of Ampere-turns. As long as the machine is not in extreme saturation, *i.e.* where dB/dH remains high, the bulk of the electromagnetic energy is stored in the air gaps of the machine between the stator and rotor. Modulation of this air gap then leads to differences in the reluctance of the machine. This salience can be utilized to produce torque when the magnetic circuit is energized by a current flowing through the winding, as outlined below.

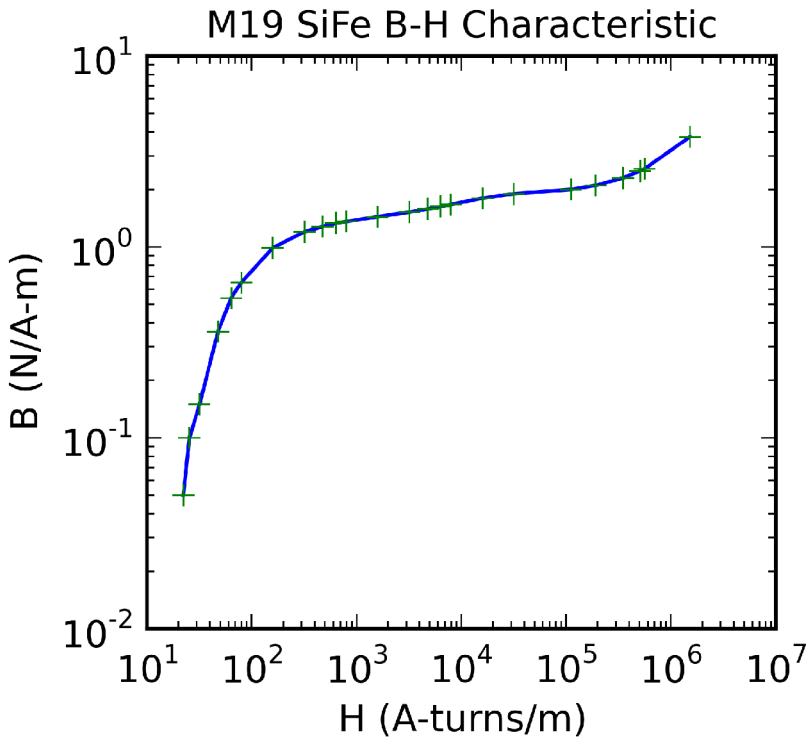

Fig. 1.2: Typical silicon steel BH curve [4].

Inductance is defined as

$$L = \frac{\lambda}{i}\,, \tag{1.6}$$

or the ratio of the flux linkage,

$$\lambda = N\varphi\,, \tag{1.7}$$

to *i*, the current required to establish the flux.

Using the definitions of flux linkage, magnetic flux and reluctance, one can provide equivalent representations of inductance as

$$L = \frac{N\varphi}{i} = \frac{N^2\varphi}{Ni} = \frac{N^2\varphi}{\oint \bar{H}\cdot d\bar{l}} = \frac{N^2\int \bar{B}\cdot d\bar{A}}{\oint \bar{H}\cdot d\bar{l}} = \frac{N^2}{\Re}\,. \tag{1.8}$$

These various relationships provide different insights as to how the geometry and construction of a magnetic circuit give rise to its electrical properties in circuit operation.

The governing equation for the electrical behavior of a phase winding can be expressed as

$$v = Ri + \frac{d\lambda}{dt}\,. \tag{1.9}$$

where *v* is the voltage between phase terminals, *R* is the electrical resistance of the phase; as such it is the sum of Ohm's and Faraday's laws. In terms of "normal" circuit parameters, this can be re-written as

$$v = Ri + \frac{d}{dt}(Li)\,. \tag{1.10}$$

As the machine moves, the reluctance of the machine varies, and therefore the inductance. Moreover, the reluctance of a path also depends upon the degree of magnetic saturation present in the system, for the relative permeability of the magnetic material is usually not a constant. Therefore inductance is a function of both position and current,

$$L = f(\theta, i) . \tag{1.11}$$

For a rotary machine, one can write

$$v = Ri + \omega \frac{dL}{d\theta} i + \frac{dL}{di} \frac{di}{dt} + L \frac{di}{dt} . \tag{1.12}$$

The magnetic energy stored in an inductor is

$$U = \frac{1}{2} L i^2 \tag{1.13}$$

and the torque provided in a rotary machine is the change in energy per change in angular position,

$$T = \frac{1}{2} \frac{\partial L}{\partial \theta} i^2 . \tag{1.14}$$

So it can be seen that torque is related to the change in inductance (and thereby the reluctance) per change in position.

1.2 Idealized RM

The ideal, linearized reluctance machine is represented by a trapezoidal inductance characteristic without consideration for magnetic saturation, core losses, or other losses. If these assumptions are maintained, then the phase excitation, with voltage *V_n*, current *I_n*, and electrical power *P_n*, shown in Fig. 1.3, gives rise to a constant current during the region of rising inductance, and thereby a constant torque in that region (Fig. 1.4). Appropriate parameters for the trapezoid will allow the torque profile of multiple phases to be combined and produce a net constant torque output for the machine. For a system operating at constant speed, this also leads to a constant mechanical power delivered by the machine.

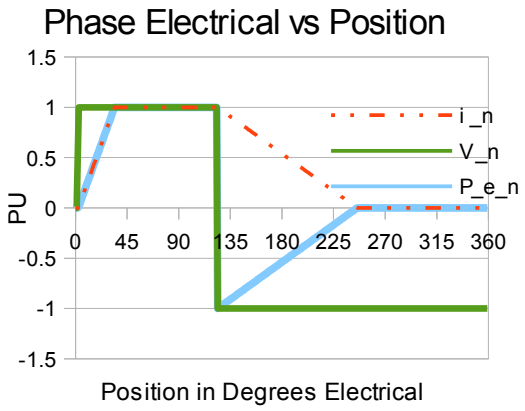

Fig. 1.3: Idealized DSRM allows simple phase excitation strategy.

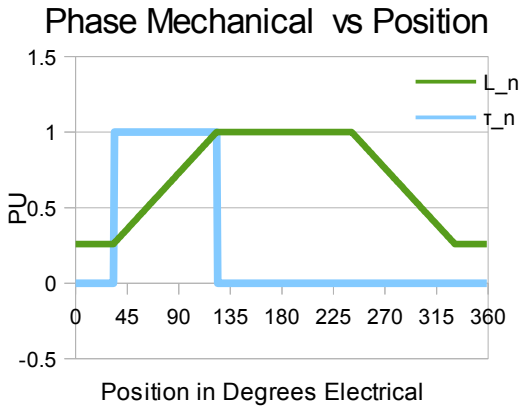

Fig. 1.4: Idealized DSRM produces constant torque with excitation from Fig. 1.11.

In such a contrived system, the phase excitation is also greatly simplified. In the motoring region, for example, a positive voltage will establish the current, reaching the desired level at the onset of the torque-producing region, where that voltage is also sufficient to maintain the current against the emf in the phase during the torque-producing region. At the end of the torque-producing region, an equal and opposite voltage is applied to quench the phase current before the machine enters the region of negative torque production. There is more inductive energy present at the end of the torque producing region than at the start, so the current takes much longer to return to zero than the time it took to establish the current.

1.3 Power Ripple in RMs

In conventional SRM implementations, both the electrical and mechanical power waveforms have strong components at the phase frequency and its harmonics. These harmonics are undesirable for a number of reasons and failure to address them adequately can lead to catastrophic failure of the system. In this section, the origins and of power ripple and its implications for system implementation are explored; measures to mitigate the effects of power ripple in literature are presented; and efforts to reduce power ripple presented in literature. The need for reducing and eliminating power ripple has been highlighted in literature [5], but up to this point a reductionist approach has been applied to address only one aspect: either mechanical or electrical power ripple.

1.3.1 Mechanical Power Ripple: Origins and Solutions

Substantial effort is required to reduce or eliminate torque ripple. Fig. 1.5 shows typical torque ripple simulated in FEA for several machines with phase excitation modeled after conventional hysteresis control. Although the linearized RM can be contrived to produce constant torque, in practice a trapezoidal inductance profile cannot be achieved as the discontinuity in the second derivative of the trapezoidal phase inductance cannot be met in the physical world. Additionally, the effects of magnetic saturation mean that practical implementations frequently have significant torque ripple – on the order of 50% or greater. In DSRM literature, the pole combination *M/N* denotes the number of stator and rotor teeth, so the 4/2 combination is a two-phase machine with four stator poles and two rotor teeth; 6/3 is a two-

phase machine with six stator poles and three rotor teeth; 12/6 is a two-phase machine with twelve stator and six rotor teeth. This torque ripple is problematic, as it places additional mechanical stress on drive train components [6] and contributes to acoustic noise [7].

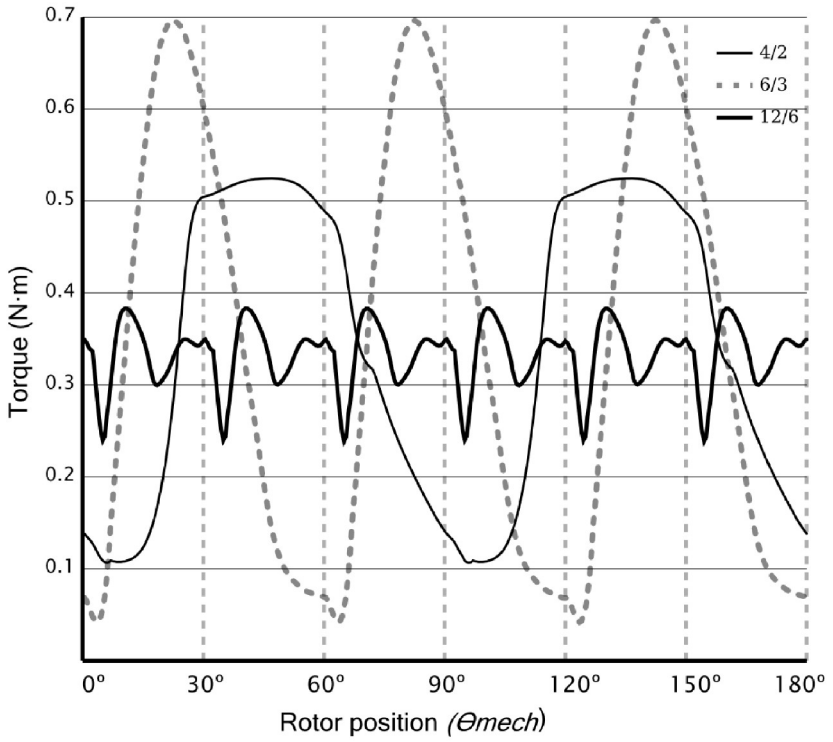

Fig. 1.5: Typical SRM torque ripple from FEA for three machines with the same average torque output.

The question arises, then, as to what mechanisms can be utilized to reduce ripple in the system torque and mechanical power. From Eq. 1.14, it is evident that the torque may be affected through the geometry of the machine and the current waveform in the phase winding. The rest of this section is devoted to outlining the major works that have investigated this issue, beginning with study of the relationship between machine geometry and torque profiles.

The fundamental parameters for producing a geometry with minimum torque ripple come down to selection of the rotor and stator pole arcs and the number of poles in the machine [8–

14]. Although it is usually the case, the pole arcs need not be uniform for all of the poles on the rotor [15] or stator [16] structure (Fig. 1.6). Tapered or wedge-shaped stator poles delay magnetic saturation in the stator and leads to a wider torque producing region (Fig. 1.7). The increased width increases the region in which multiple phases to overlap, allowing for multi-phase excitation to mitigate torque ripple [17–21].

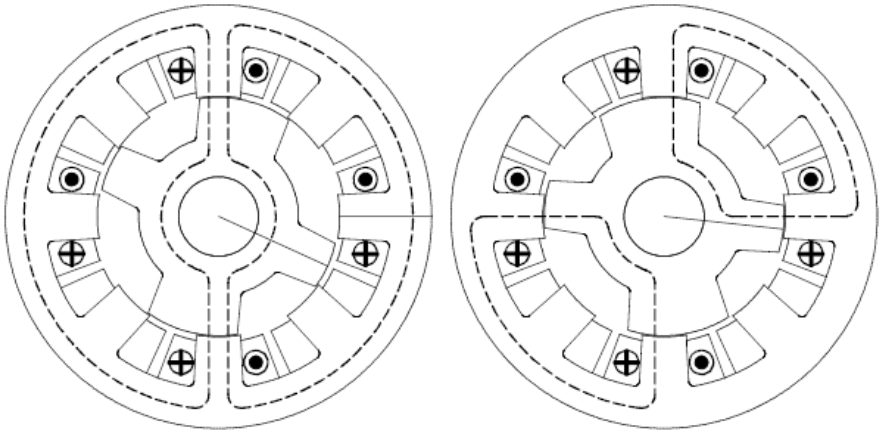

Fig. 1.6: Varied rotor pole widths [15].

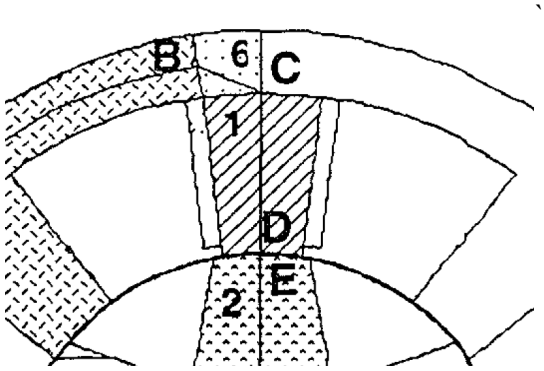

Fig. 1.7: Wedge-shaped stator pole [17].

In addition to the basic pole geometry, the torque profile may also be modified by altering the pole face. Modifications to the face alters the length and width of the effective air gap and reluctance of the magnetic circuit. Several modifications have been proposed in literature to

pursue various aims. Rectangular sections were subtracted from the leading edge and added to the trailing edge of the poles in [22], (Fig. 1.8). A similar notch was made in [23], where the notch was in polar coordinates (Fig. 1.9). The use of a full-width tapered, saw-tooth, and partially chamfered profiles on rotor pole faces under constant-current excitation was investigated in [12]. (Fig. 1.10) Although it is not clear if the variation was in the Cartesian or polar coordinate system nor the effect on net machine torque ripple in this work, stator poles which are linear in Cartesian space are presented in [24]. A linear relationship between pole radius and angular position was presented in [25] (Fig. 1.11) and non-concentric arcs were used in [26] (Fig. 1.12). In [27], continuously graded pole surfaces and air gap profiles with a continuous first derivative (Fig. 1.13) are claimed as inventions, but no indication were provided as to exactly how the surface was to be specified to achieve zero torque ripple. Moreover, their claims were undermined through all of the included artwork, showing stator poles geometries which introduce a discontinuity to the air gap.

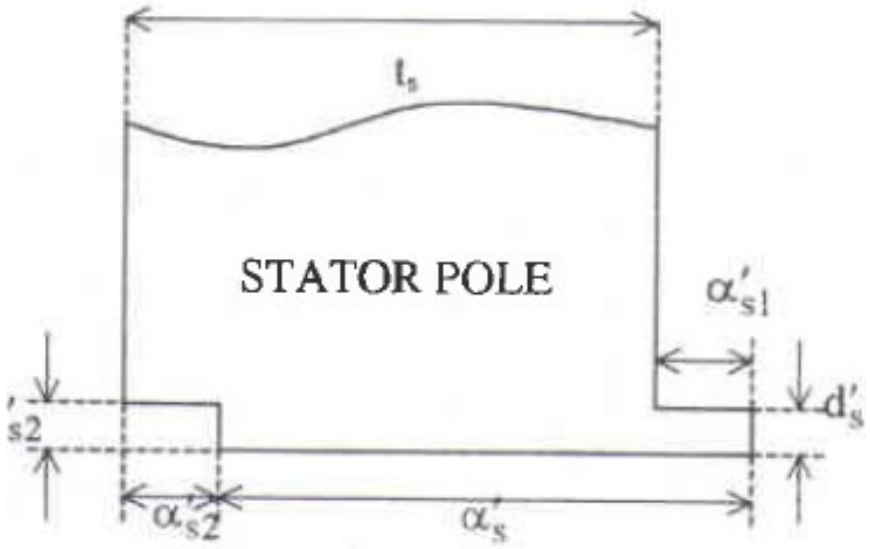

Fig. 1.8: Rectangular void at leading edge and addition at trailing edge [22].

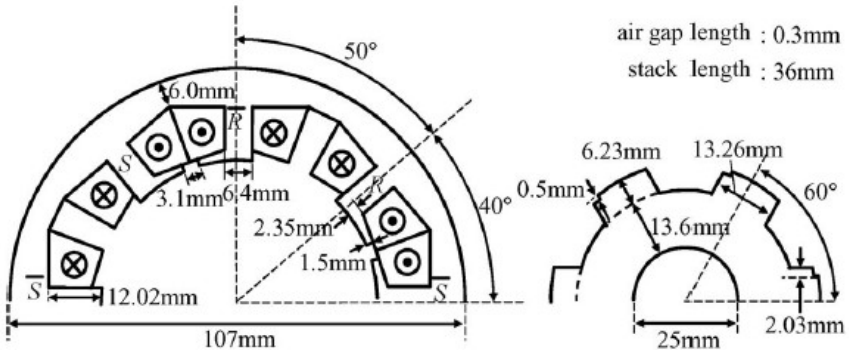

Fig. 1.9: Rectangular cutout on rotor pole [23].

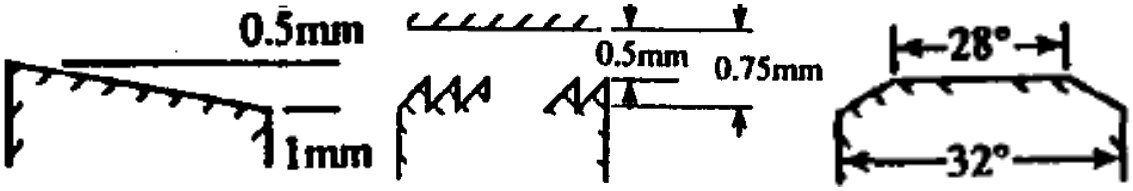

Fig. 1.10: Three pole profiles: tapered, sawtoooth, and chamfered. [12].

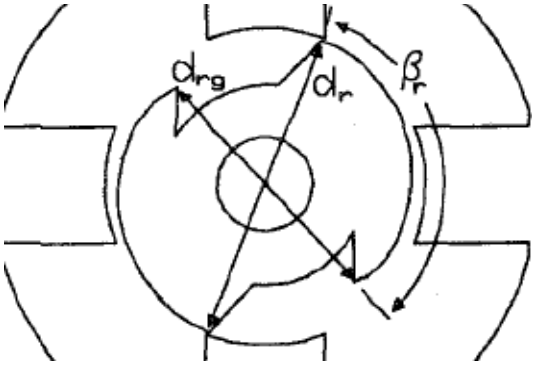

Fig. 1.11: Notch on pole side and linear r vs theta on face. [25]

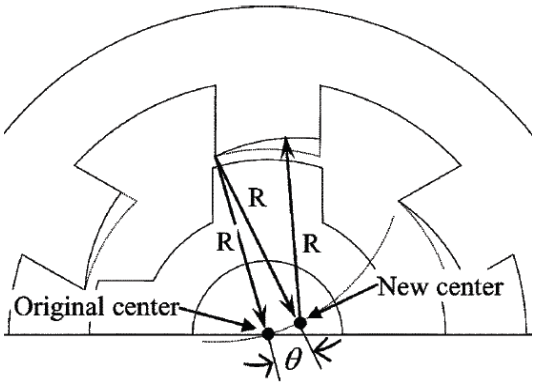

Fig. 1.12: Pole face from non-concentric arc. [26]

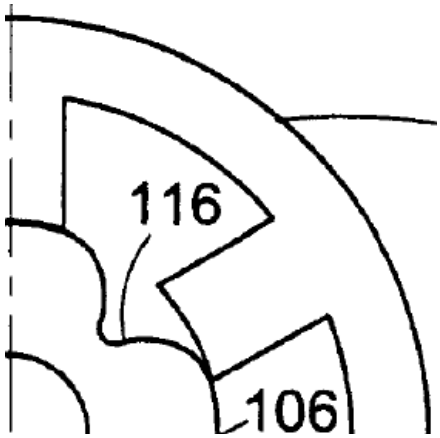

Fig. 1.13: Continuous first derivative in rotor surface [27]

The torque profile may also be affected by introducing a void in the side of the pole (Fig. 1.14), as described in [25], [28], [29]. The voids may also be moved to be completely enclosed by the lamination (Fig. 1.15) and filled by a material with a lower permeability, either air or some other magnetic material [29–31]. However, these methods are considered inferior as they increase the amount of electromagnetic material operating in deep saturation, increasing core loss and reducing overload capacity.

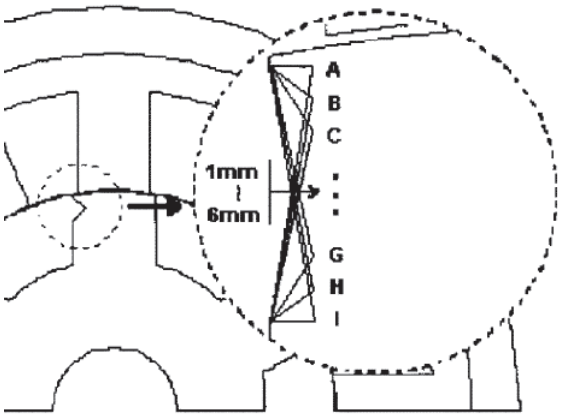

Fig. 1.14: Notch on side of rotor pole. [25]

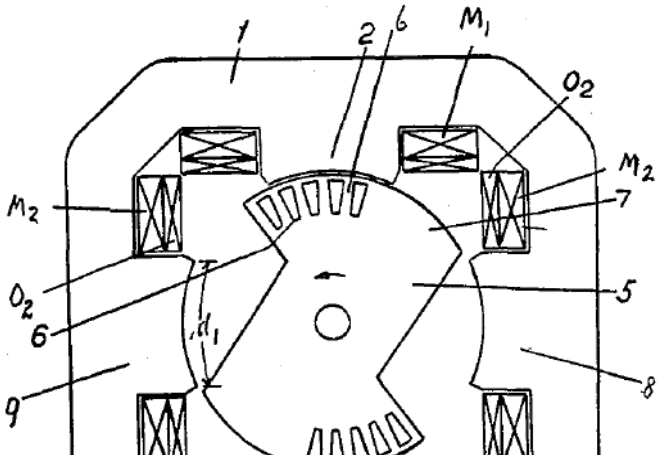

Fig. 1.15: Interior void on rotor. [29]

The torque ripple may also be reduced by skewing multiple sections [32] or individual laminations [12] within the machine, but the complexity of construction makes these options less desirable. All of these efforts either do not propose a method or algorithm by which the various devices can be used to shape the inductance profile, or they use a crude guess-and-check method to minimize torque ripple by varying one or two of parameters on some preconceived feature. Due to these limitations, these methods for manipulation of machine geometry have not been

shown to be successful in eliminating torque ripple, merely a reduction in torque ripple is possible.

Once a machine's geometry is fixed, the phase control is the only method by which the torque can be controlled. In some instances, a high-frequency torque transducer was incorporated into the system and utilized as an input to the controller in order to minimize torque ripple [33], [34]. However, the usual course is to forgo the extra expense and complexity of physical torque sensor and estimate the torque ripple by modeling the torque characteristic of the machine and controlling the phase currents according to the model. A brief summary of such modeling and control techniques follows.

Torque control for robotic servo applications was proposed in [35], [36], where feedback linearization of the system was utilized to select a single phase and current magnitude to produce the reference torque. In the same period, multiple phase currents were utilized in brushless permanent magnet dc machines to achieve the reference torque [37], [38]. Feedback linearization and multi-phase excitation were quickly combined in [39–42]. The relationship between torque, rotor position, and phase currents could be obtained through model [43] or through experimental techniques [44]. Depending upon the situation, the relationship could be computed while the system was running or precomputed, stored, and utilized in online system control.

For precomputed approaches, numerous methods have been used to optimize the computation or memory requirements for looking up the desired operational point, including fuzzy adaptive systems [45], [46], neural networks [47], [48], spline interpolation functions [49]., or their harmonic content [50–52].

In multi-phase excitation, several combination of phase currents can produce the desired torque output, providing an added degree of freedom to the system controller. Do arrive at a deterministic output, torque sharing or distribution functions have been proposed [42], [53], [54]. The particular operating point may be selected to minimize conduction losses within the machine [55–58], but this does not consider losses incurred elsewhere in the system, such as magnetic core losses or power source losses. Other works have sought to unify the operation of RMs with inductance or PM machines by controlling a stator flux linkage vector, through which a form of direct torque control can be utilized [59], [60].

Current control of torque, however, can have unpredictable effects upon machine efficiency and the system's electrical power ripple. In these regards, it is more desirable to have a machine whose geometry is designed for minimum torque ripple for a given excitation. Effective control of torque ripple over a wide speed range is also difficult due to saturation in the voltage-source inverters, as noted by several works.

It is desirable, therefore, for the design process to consider the influences of both the machine geometry and excitation. Designing the geometry in isolation may result in saturation of the drive electronics and control, resulting in the persistence of torque ripple and loss of efficiency in the electronics. Similarly, isolationist design of control may result in sub-optimal utilization of the magnetic material by either over-driving to compensate for low torque production or under-driving where high torque production could be taken advantage. Only one work of note has been found where both geometry and excitation have been considered in the design phase, although this has been in a permanent magnet flux-reversing machine [61].

Clearly, there is a dearth of data on this aspect of RM design which will be addressed in Chapter 2.

1.3.2 Electrical Power Ripple: Origins and Solutions

Contrary to the mechanical power, the net electrical power in the ideal machine under conventional excitation is not constant. In particular, there is a large discontinuity at the point where the voltage switches from positive to negative. Even when several phases are combined, the peak-to-peak power ripple in the machine is several times larger than the average electrical power. In Fig. 1.16, *P_e_n* is the electrical power within one phase of a four-phase machine. Combining the power for all of the phases result in a net machine electrical power, *P_e*, which demonstrates a large ripple in the electrical power, which is directly proportional to the current flowing into the machine for a system operating from a voltage source. Therefore the input current drawn by the system will also have a large discontinuity.

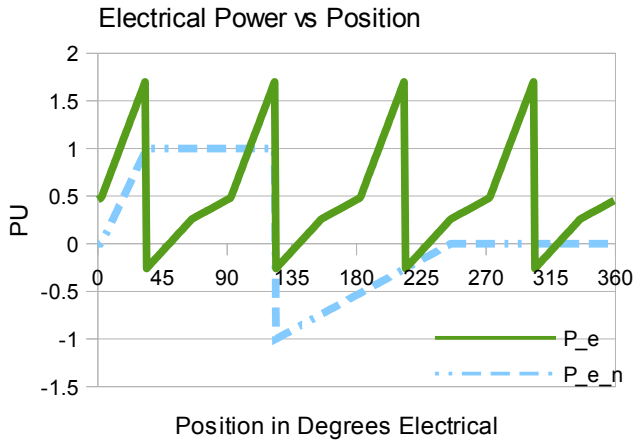

Fig. 1.16: Net electrical power (green) sees a large peak-to-peak ripple and discontinuity under conventional excitation.

One consequence of having a large current ripple is that the resistive losses in the source and transmission line are proportional to the rms current, which will be larger than the average current. This results in increased heat dissipation and loss of electrical efficiency in the supply and require larger components ratings in the source, increasing size, weight and cost. Moreover, if the source has an inductive element, either manifested in a physical component or control algorithm, the discontinuity in the current leads to a large power surge within the drive electronics. If this surge is not properly controlled, the excess energy can lead to over voltage and failure of the drive electronics.

This characteristic of conventional SRM implementation has been taken as a fundamental property of RMs. The subsequent incorporation of a large capacitor bank into the drive electronics has been the generally accepted method to address the electrical power ripple for nearly three decades [62]. In practical terms, this required the employment of aluminum electrolytic capacitors, which have the highest volumetric capacitance and lowest cost for large values. The weaknesses of electrolytic capacitors are that they have a shorter life time and higher equivalent series resistance compared to other capacitor technologies, such as metalized film.

Only within the last few years have there been investigations into the reduction of electrical power ripple in SRMs. In [63], a blocking diode was introduced to prevent power flow from the drive to the source (Fig. 1.17). To prevent an over-voltage condition within the drive, the duty cycle applied to the enervating phase (phase n) was manipulated such that the power returned from phase n is balanced with the power drawn from the energizing phase (phase $n+1$),

$$d^n = \frac{i^{n+1} d^{n+1}}{i^n} . \qquad (1.15)$$

where d^x is the duty cycle ratio for phase x and i^x is the current in phase x.

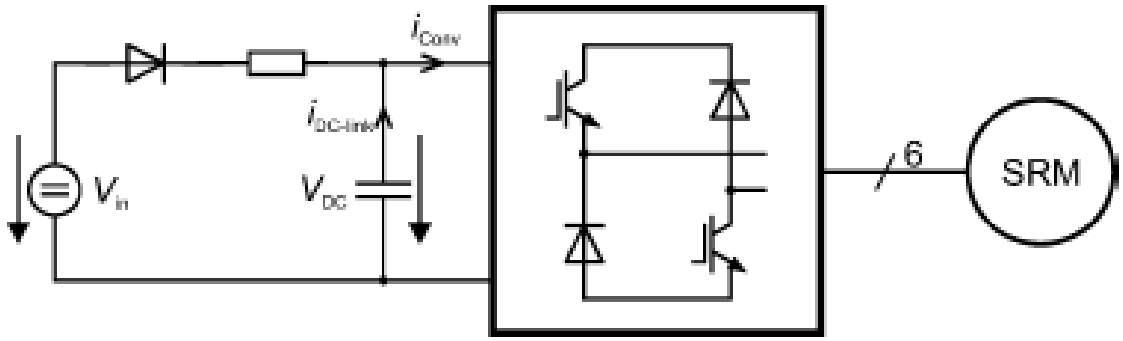

Fig. 1.17: A blocking diode in the drive prevents negative supply current [63].

This has the effect of introducing long tail currents to the phase excitation (Fig. 1.18, top), and showed good results for low (100 rpm) and rated (3500 rpm) speeds in simulation. However, this technique demonstrates a current demand on the power source that is discontinuous (Fig. 1.18, bottom), which arises from an oversight in the formulation of the control law which regulates the net bus current at zero. A reformulation of Eq. 1.15, allowing for constant converter current, would appear as

$$d^n = \frac{i^{n+1} d^{n+1} - i^{bus}}{i^n} . \qquad (1.16)$$

where d^x is the duty cycle ratio for phase x and i^x is the current in phase x, and i^{bus} is the reference current to be drawn from the supply.

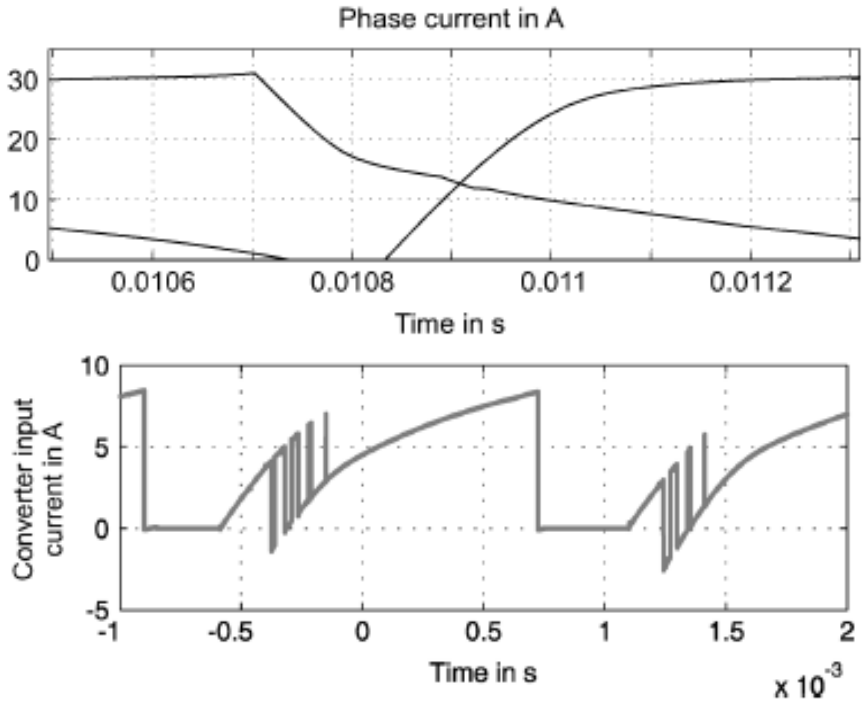

Fig. 1.18: The control method described in [62] adds long tail currents to the outgoing phase (top), largely avoiding negative current from the course (bottom).

Torque and mechanical power ripple was not investigated in simulation or experiment. Furthermore, the circuit topology prevents bidirectional power flow in the system, thus limiting the scope of its application to those that do not require both motoring and braking. The authors have also investigated a similar commutation strategy in which the gating signals for each phase have hysteresis controllers to based on both phase currents and bus voltage [64].

In [65], the blocking diode was replaced by an LC filter (Fig. 1.19). The control strategy is to perform high-bandwidth sensing and integration of the bus current on a cycle-by-cycle basis under PWM control. Three operating regions are described: 1) conduction of a single phase; 2) commutation between two phases where the outgoing phase current is larger than the incoming

phase current; and 3) commutation between two phases where the outgoing phase current is less than or equal to the incoming phase current.

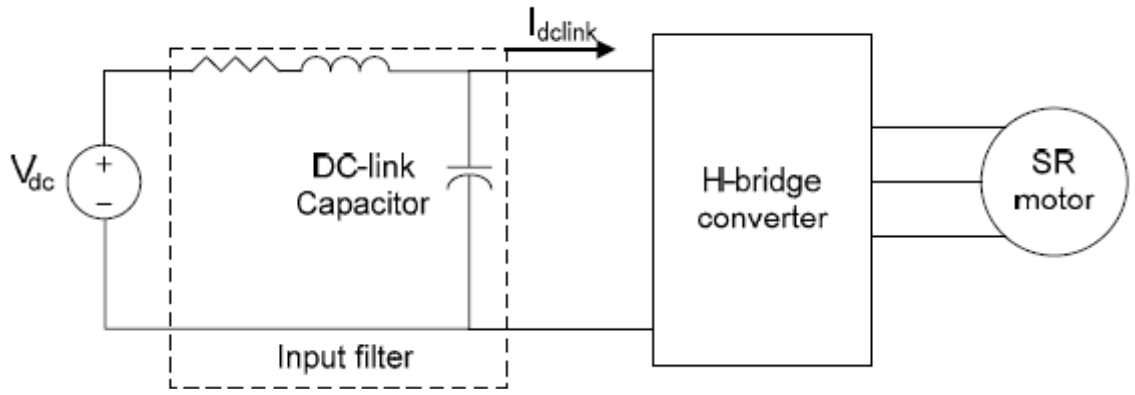

Fig. 1.19: LC-filtered source input in [64].

In mode (1), a positive voltage vector is applied to the phase winding until the integration of the phase current achieves a threshold value, at which point a zero voltage vector is applied and the phase current freewheels, contributing no net current to the source current. The integrator is reset at the beginning of the next PWM cycle. In mode (2) a negative voltage vector cannot be applied to enervate the outgoing phase until the current in the outgoing phase is less than that of the incoming phase – a zero voltage vector must be applied and the phase current freewheels without a net contribution to the bus current. During this time, the gating of the incoming phase is performed as in mode (1). In mode (3), the PWM cycle commences by a simultaneous application of a negative voltage vector applied to enervate the outgoing phase and a positive voltage vector applied to energize the incoming phase. As the energizing phase current is greater than the enervating phase current, the integrator value rises. If the integrator reaches the threshold, a zero-voltage vector is applied to both phases. Simulation results for the commutation strategy showed promise for controlling the low-frequency capacitor bus voltage excursions, but

the output torque of the modeled machine exhibited significant torque ripple. Moreover, the technique was only simulated at less than 30% of the machine's rated output.

Following this control method, the bus current will never exceed the a maximum set by the threshold. However, there is no guarantee that the threshold will be satisfied, which would lead to dips in the current drawn from the supply. By way of example, if the energizing phase current does not rise quickly enough in the latter modes, the integrator threshold will not be met. This condition is and are visible in the trace I_{dclink} shown in Fig. 1.20. Furthermore, if the current in the outgoing phase enters the regenerative region, the restriction of the voltage applied in modes (2) and (3) can lead to a large negative torque production, which was noted by the authors.

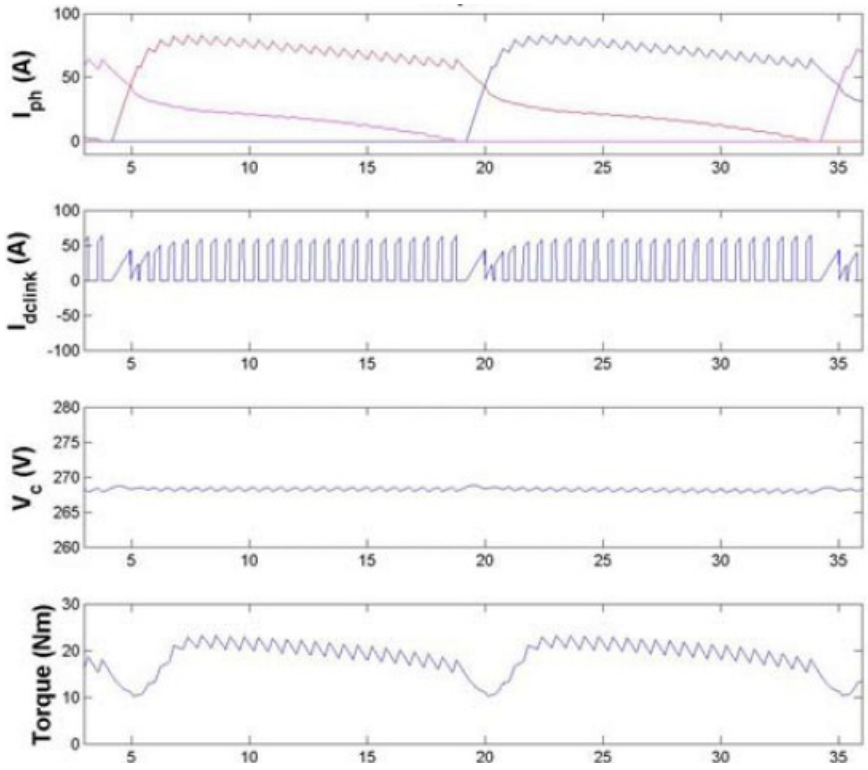

*Fig. 1.20: S*imulated wave forms at 30% of rated power in [64].

Even with the implementation of the control schemes in this section, the machine in use may yield unsatisfactory results in efficiency, converter current ripple, and torque ripple. However, these publications illustrate the feasibility of controlling the power delivered to the phases so that the bus current and power are much closer to a dc value through the controlled commutation of the incoming and outgoing phases. Further work on this subject is warranted and will be addressed in Chapter 3.

1.3.3 Combined Power Ripple: Solutions

As outlined previously, design of machine and control for DSRM systems are performed independently, despite the fact that the ultimate system performance has many inter-dependencies between the two. A similar reductionist approach is taken to the problems of ripple in the flow of electrical and mechanical power through the system. It may be no surprise, then, that there are no works in literature that simultaneously address ripple in torque and mechanical power, *i.e.* net machine current and torque. Chapter 4 addresses this deficit.

1.4 Summary

As this chapter illustrates, the power ripple in conventional DSRM systems present significant challenges to their implementation and acceptance in the marketplace. To date, the attempts to address this issue are limited in scope and even then are of limited success while the effects on other performance aspects are unpredictable and frequently detrimental. A unified approach to addressing the problems of mechanical and electrical power ripple is needed, taking both the machine geometry and control into consideration at the design phase, but not to the detriment of efficiency and cost. The following chapters provide algorithmic approaches to eliminating power ripple emanating from the system that can be utilized independently or concurrently during design. With their combined use, a machine can be produced with power ripple contained within a desired bound.

Chapter 2: Reluctance Shaping

The concept of shaping the inductance profile through modification of the machine geometry is not new, but up to this point has been a rather haphazard affair. This chapter presents a method which relates the effect of changes in the air air gap geometry upon the torque profile for a given phase excitation, then utilizes that relationship to modify the torque-position curve in a predictable manner by altering the geometry of the pole face. In this manner, deviations of the torque from its mean value can be characterized and eliminated, the result of which is a machine geometry which reduces or eliminates ripple in the torque and mechanical power from the machine.

At a basic level, a mapping is generated between a perturbation of the air gap profile and the resulting perturbation to the torque profile. Once a map exists, the ripple component of the torque profile is isolated and modeled using an approximation function. The perturbation map is then utilized to generate a modification to the air gap profile which should cancel a portion of the torque ripple. The following sections will address the exact details of the process.

2.1 Geometric parametrization

Previous works have defined only one or two parameters related to a feature on the pole face and a guess-and-check method was utilized to find different, nearby parameter value which reduced torque ripple, which was then incorporated in the next iteration as the seed value. While these methods do reduce torque ripple, they do not eliminate it completely. For complete elimination, a continuous variation of the pole face is needed.

Moreover, it is not known *a priori* as to what pole geometry will satisfy the torque ripple requirements. Therefore, the candidate for pole modification cannot be as simplistic as previous attempts, *e.g.* a linear variation of the pole face or non-concentric arcs. Therefore, we will define the pole face as

$$r = f(\theta) \tag{2.1}$$

where the radius r is an indeterminate function, f, with respect to the angular position, θ.

In this implementation, Ansys' Maxwell 2D Finite Element Analysis (FEA) is utilized to model and simulate the electrical and electromagnetic circuits of the machine and the electronic drive. In FEA, the machine geometry is approximated with a finite number of nodes, both within a given geometry and at the surface of that geometry. It is natural, then, to parametrize the discrete locations of the surface forming the pole face. This discretization produces the desired result of a large number of parameters available for modification in the search for a pole geometry providing a suitable torque characteristic. The number of samples in the discretization should be sufficient to allow the sampled points to closely approximate a curved surface, but an

overly large sample size results in a higher computational requirement without increasing the fidelity of the model. For this model, a sample size of 100 was chosen.

In conventional DSRMs, the rotor pole arc is typically selected to be greater than that of the stator pole, *i.e.* the rotor poles are wider than those of the stator. In that case, variations in the air gap profile would be manifested in a rotor pole face which is non-concentric with the central axis of the machine. In this work, however, the stator poles have been selected to be wider than those of the rotor. Therefore, the air gap variation is reflected in the stator pole geometry as:

$$r_i = f(\theta_i), i \in [0, 100) \tag{2.2}$$

In the machine, there is a minimum air gap,

$$l_{g,min} = r_{s,min} - r_{r,max} \tag{2.3}$$

where $r_{s,min}$ is the minimum inside radius of the stator pole face and $r_{r,max}$ is the maximum outer radius of the rotor pole. This minimum gap has a physical constraint on its lower bound due to the tolerances of the manufacturing process and mechanical assembly. From the standpoint of electromagnetics, it may be desirable to have a minimum airgap that exceeds the physical limit in some situations. In any case, the parametrization of the pole face can be re-written in terms of these physical constraints

$$r_s(i) = r_{s,min} + l_{g,min} g(i) \quad . \tag{2.4}$$

where the gap function, $g(i)$, is a unitless quantity and is positive semi-definite so as to not violate the minimum air gap constraint. The initial parametrization was chosen to be a piecewise linear ramp:

$$g_0(i)=\begin{cases}1.05-\dfrac{1.05}{60}i & i\in[0,60)\\ 0 & i\in[60,100)\end{cases}. \tag{2.5}$$

In other words, the air gap roughly doubles from it's minimum to the maximum, as the radius of the pole face is decreased by 1.05 times the minimum air gap, and there are forty points on the pole face with constant radius.

The second coordinate of the node location, its angular position θ, was simply defined as a uniform distribution across the pole face,

$$\theta(i)=\frac{\beta_{sp}}{100}i\ , \tag{2.6}$$

where β_{sp} is the width of the pole face in degrees.

In this manner, location of each node on the pole surface is given in polar coordinates by

$$n[i]=(r[i],\theta[i])\ . \tag{2.7}$$

This initial pole profile is based on previous experiences in DSRM design and provides a faster convergence than starting from a flat, constant radius pole face.

2.2 Perturbation process

The discretization of the pole profile produces a large number of parameters, as per the stated goal. Due to this explosion in parameters, the algorithms presented in literature are not efficient methods for determining which parameter variations will reduce torque ripple. What is needed is a method to identify the affect of changes in the gap function *g* to the torque profile of the machine and an invertible map between changes in gap and torque. In the following subsections, a method is presented that establishes a cause-and-effect relationship between perturbations to the gap function and the FEA calculation of torque production. In addition to modeling the dynamic electromagnetic fields in the machine, Maxwell 2D also has the ability to perform limited SPICE circuit simulations so that the actual phase excitation and mechanical frequency are considered when modeling the machine's torque production.

2.2.1 Gap perturbation

With the pole surface parametrization provided in the previous section, the gap function, *g*, is perturbed with a Gaussian distribution,

$$\Delta g(i) = a\, e^{-\frac{(i-\mu)^2}{\sigma^2}}, \tag{2.8}$$

where *a* is the amplitude of the perturbation, μ is the center of the perturbation, and *σ* is the width of the perturbation. The perturbed tooth profile, g_{n+1}, is then

$$g_{n+1} = max\left(g_n + \Delta g(a, \mu, \sigma), 0\right) \tag{2.9}$$

where the *max* function is needed to preserve the positive-semi definite property of the gap function.

Fig. 2.1 illustrates the modification of the gap function, showing the original gap, perturbed gap, and the perturbation. Due to the non-linearity inherent in the electromagnetic circuit, the amplitude of the perturbation, a, should be kept small. The perturbation center, μ_i, must also be constrained to be within bounds of the pole. The perturbation width, σ, must also not be too large for proper identification of the torque perturbation.

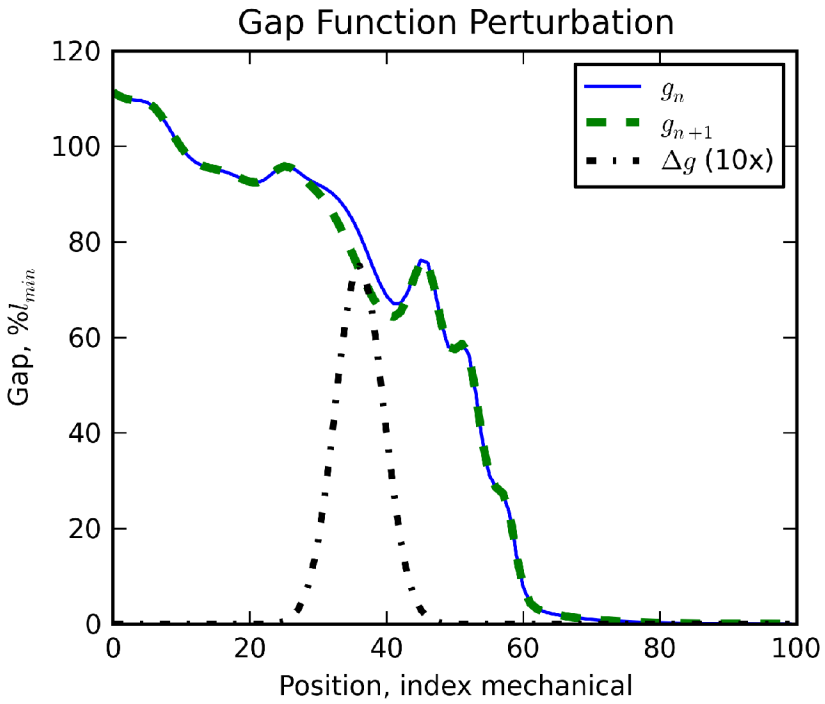

Fig. 2.1: The original and modified gap function, due to a Gaussian perturbation.

2.2.2 Identification of torque perturbation

Once the pole profile is perturbed, FEA is utilized to model the phase torque of the perturbed pole profile, T_{n+1}. Fig. 2.2 illustrates phase torque responses of the initial radius (T_n) and perturbed (T_{n+1}), in addition to the delta. Ansys' Maxwell 2D can simulate with the actual

phase excitation profile through a built-in SPICE simulator. For this design, the excitation was similar to that of a hysteresis-controlled current – a constant-voltage rise, current sustain, and constant-voltage fall. Only one phase is energized, otherwise the effects of the perturbation are manifested multiple times within an electrical cycle, inhibiting the identification of the perturbation parameters. During FEA simulation, the torque profile is sampled at discrete time steps, which correspond to discrete rotor positions. As the angular velocity of the rotor is fixed, the discrete time samples also correspond to uniformly-spaced positions.

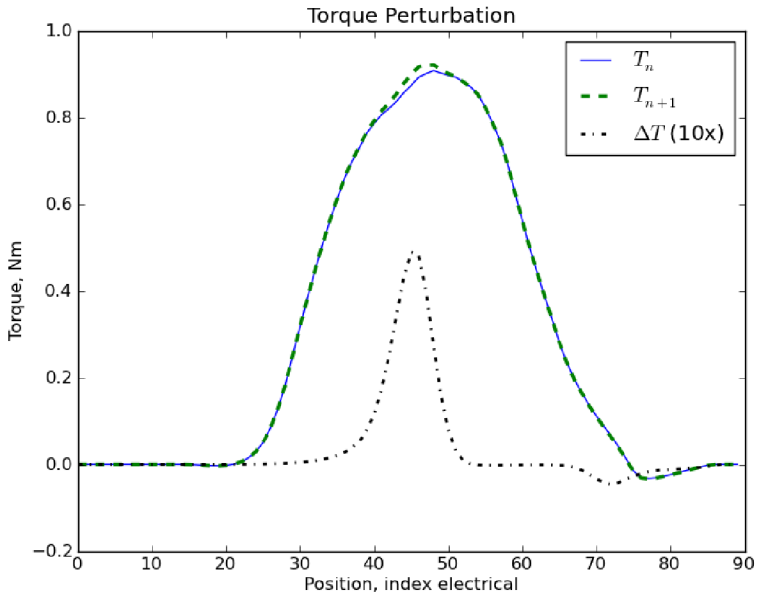

Fig. 2.2: The original, modified and perturbation of the phase torque due to a Gaussian perturbation of the gap function, g.`

With sufficient simulation time, a complete phase excitation cycle is modeled and exported for analysis. The torque perturbation is calculated as

$$\Delta T = T_{n+1} - T_n \tag{2.10}$$

With the torque perturbation isolated, it can be modeled in a manner similar to the radius perturbation. We can see that the torque perturbation has two displacements of opposite sign that are produced when the radius perturbation enters and exits the region of overlap between the rotor and stator pole faces. These two displacements can be modeled as the sum of two Gaussian-distributed perturbations. In order to accomplish this, the torque perturbation displacements are isolated and modeled independently. It is assumed that the torque perturbation has two distinct excursions of opposing signs and each Gaussian identification matches to either the maximum or the minimum peak of the input signal. If the width of the gap perturbation is too great, this assumption is invalid and the torque perturbation will be difficult to characterize.

To identify the center of the Gaussian distribution, several transformations of the signal were performed. First, the location of the peak of the signal was identified,

$$s_0(i) \le s_0(i_{pk}) \quad , \tag{2.11}$$

where *i* denotes the index of the sampled signal.

First, the absolute value of the signal was taken, then the signal was bounded at a minimum value, ϵ :

$$s_1(i) = max\left(|s_0|, \epsilon\right) \quad . \tag{2.12}$$

Next the natural logarithm of the signal was taken,

$$s_2(i) = \ln\left(s_1\right) \quad , \tag{2.13}$$

shifted,

$$s_3(i) = s_2(i) - s_2(i_{pk}) \quad , \tag{2.14}$$

and the square root was taken,

$$s_3(i) = \sqrt{s_2(i)} \quad . \tag{2.15}$$

Since the Gaussian distribution has a x^2 term in it, this functions as an absolute value. So, finally, the sign was inverted for the values to the left of the peak index,

$$s_4(i) = \begin{cases} -s_3(i) & i < i_{pk} \\ s_3(i) & i \geq i_{pk} \end{cases} \tag{2.16}$$

If this result is performed on a Gaussian distribution, a simple line results, although the curve has zero slope in the region where the input signal was clamped according to Eq. 2.12. From this line, it is a simple matter to perform a least-squares fit to identify the slope and the x-axis intercept. The slope corresponds to the width parameter, σ, and the x-axis intercept corresponds to the center index of the Gaussian distribution, i_μ,

$$\vec{a} = \left(\vec{i}\, W\, \vec{i}^{\,T}\right)^{-1} \vec{i}\, W\, \vec{s}_4^{\,T} \tag{2.17}$$

where i is the range of allowable indices, and with

$$\vec{a} = \begin{bmatrix} \sigma \\ y_0 \end{bmatrix} \tag{2.18}$$

where σ is the width of the Gaussian distribution and y_0 is the y-axis intercept.. The x-axis intercept is the center of the Gaussian distribution, found by

$$\mu = y_0 / \sigma \quad . \tag{2.19}$$

The weighting matrix W is a diagonal matrix whose elements are chosen to place greatest emphasis on the region around the zero crossing by the formula

$$W_{m,i} = \begin{cases} e^{-\frac{(i-i_{pk})^2}{(0.1I)^2}}, & m = n \\ 0, & m \neq n \end{cases} \quad , \tag{2.20}$$

where *i* is the total number of samples in the signal of interest. The magnitude of the distribution, *a*, is found by comparing the area under the curve of the input wave form with that of a prototypical distribution which with unity magnitude,

$$a_T = \frac{\sum_{n=n_{min}}^{n_{max}} \Delta T_n}{\sum_{n=n_{min}}^{n_{max}} e^{-\frac{(n-\mu_T)^2}{\sigma_T^2}}} \quad . \tag{2.21}$$

The result of this identification method for the Gaussian parameters can be seen in Fig. 2.3, which shows the original torque perturbation and its approximation by the sum of two Gaussian distributions.

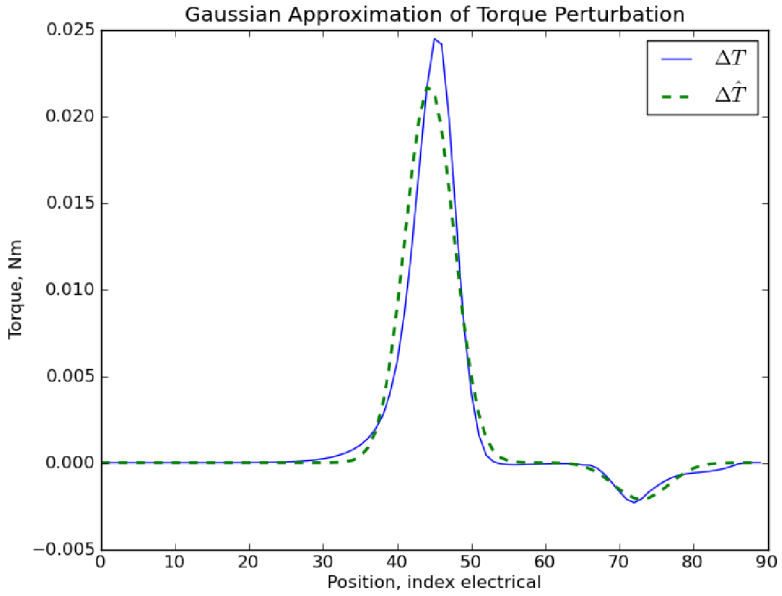

Fig. 2.3: The torque perturbation and its Gaussian estimate.

2.2.3 Gap-torque perturbation map

At this stage, the main components of the mapping are in place: a perturbation for the gap function has been formulated; the perturbation results in a perturbation to the torque profile; and a method for identifying parameters has been presented to construct a model of the torque perturbation with reasonable accuracy. The remaining piece is to establish a population of gap and torque perturbation parameters and construct a mapping between them.

A small number of perturbations can be made to the initial rotor profile to establish a sample population from which a mapping function can be built,

$$\begin{aligned}&\Delta g\left(a_g, \mu_g \sigma_g\right) \rightarrow \\ &\quad \hat{T}_1\left(a_{T1}, \mu_{T1}, \sigma_{T1}\right) + \hat{T}_2\left(a_{T2}, \mu_{T2}, \sigma_{T2}\right)\end{aligned} \quad . \tag{2.22}$$

A polynomial fit was generated to relate the gap parameters to the torque parameters: magnitude,

$$\hat{a}_{Tx} = \sum_{n \in \{N_0, N_1 \ldots\}} \alpha_{x,n} a_g^n \quad , \tag{2.23}$$

center,

$$\hat{\mu}_{Tx} = \sum_{n \in \{N_0, N_1 \ldots\}} u_{x,n} \mu_g^n \quad , \tag{2.24}$$

and width,

$$\hat{\sigma}_{Tx} = \sum_{n \in \{N_0, N_1 \ldots\}} o_{x,n} \sigma_g^n \quad . \tag{2.25}$$

where α, u, and o are the coefficients of the curve fit for amplitude, mean, and width of the distribution. The members of the set for values of the polynomial order n are determined by visual inspection and intuition. The sample populations, the polynomial approximation, and the

polynomial mapping equations are shown in Figs. 2.4-2.6. The centers of the distribution show a strong linear correlation and amplitude exhibits a reasonable correlation with a cubic polynomial.

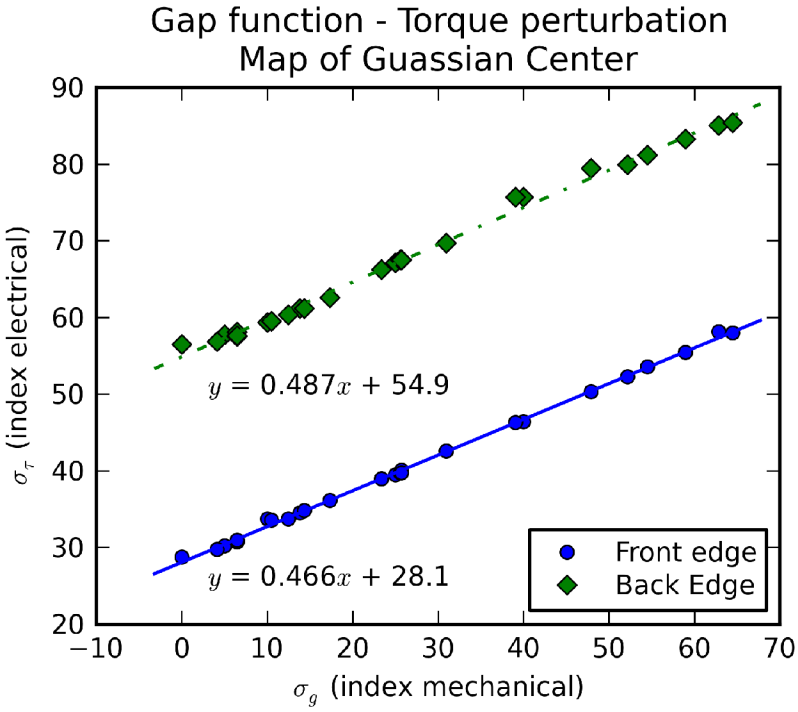

Fig. 2.4: Map between Gaussian centers.

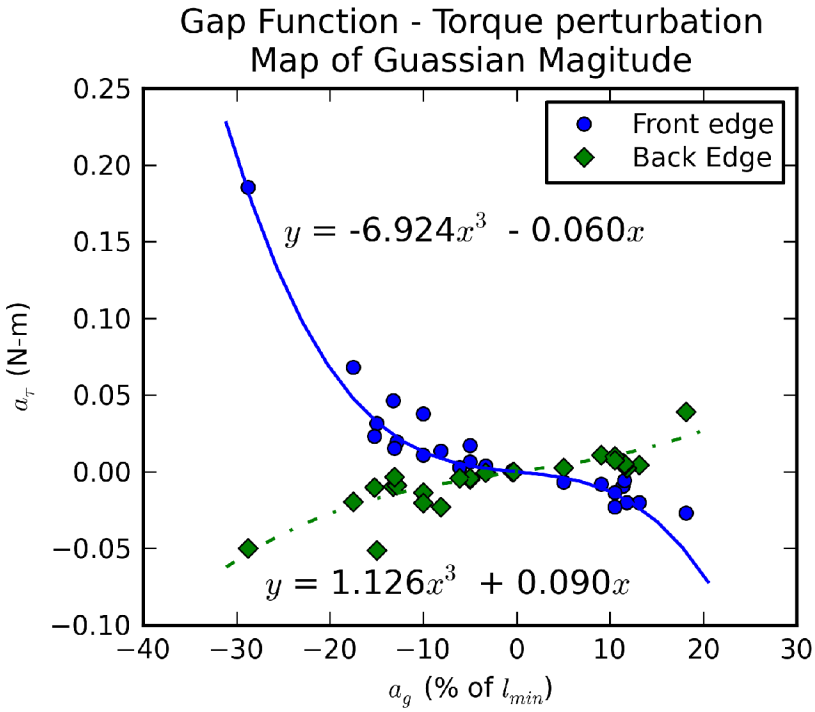

Fig. 2.5: Map between Gaussian magnitudes.

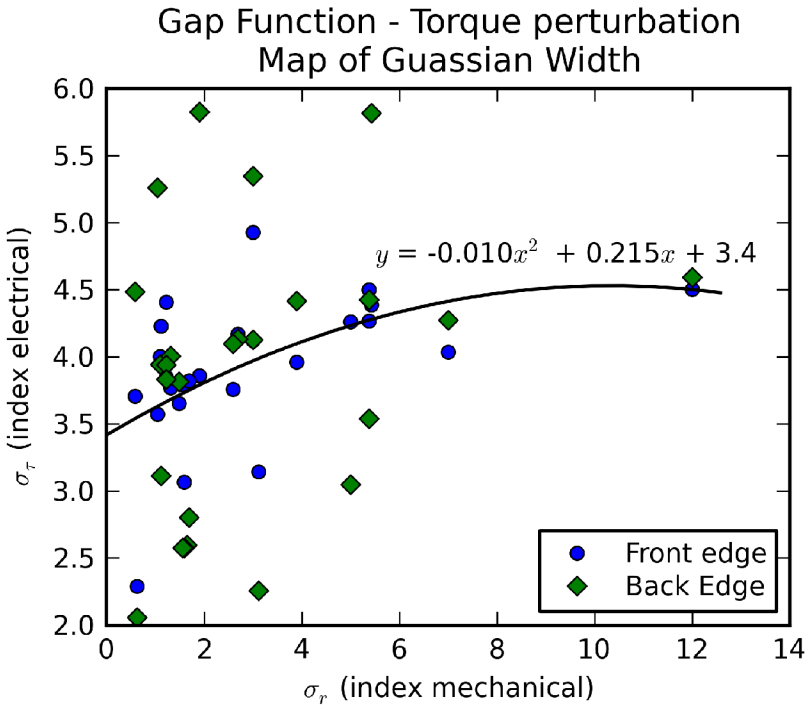

Fig. 2.6: Map between Gaussian widths.

The width of the Gaussian distribution, however, exhibits a weaker polynomial correlation than the other two parameters which can be attributed to a number of causes. For example, as the phase current is not constant, the torque response to the gap function perturbation is not uniform. Secondly, the width of the deviation could become less concentrated as the air gap increases, as a surface perturbation would become imperceptible if there is a large distance between the stator and rotor pole face. However, the correlation is sufficient to achieve the goal of reducing torque ripple, as shown in the next section.

2.3 Design study in FEA

Once a small seed population of perturbations has been established, a mapping can be constructed between the rotor and the approximated torque perturbations. In the previous section, only one phase was excited during FEA simulation. In order to reduce the torque ripple, the full-machine torque characteristic must be obtained. DSRMs are generally regarded as having phases which are independent in their inductance and torque production, *i.e.* the current, voltage, and torque on one phase does not alter those parameters on other phases. There are cases where this assumption does not hold, such as when the core is driven into saturation, which would require the simulation with all phases energized. However, for the purposes here we can simply model the net torque as

$$T = \sum_{n=0}^{N} T_n \quad , \tag{2.26}$$

where the phase torques of other machine phases can be obtained by shifting the phase of the torque signal,

$$T_n = T_0(i_0) \cup T_0(i_1), i_0 \in \left[n\frac{I}{N}, I \right), i_1 \in \left[0, n\frac{I}{N} \right) \quad , \tag{2.27}$$

where I is the total number of samples and N is the total number of phases.

Once the full torque is in hand, the desired torque signal is simply the average,

$$T^* = \frac{1}{N} \sum_{n=0}^{N} T \quad . \tag{2.28}$$

and so the error signal can be defined as

$$\epsilon_T = T^* - T \quad . \tag{2.29}$$

Some portion of the error signal can then be approximated with a Gaussian distribution, *e.g.* the largest deviation from zero,

$$|\epsilon_\tau[i_{max}]| = max\left(|\epsilon_\tau[i]|\right) \quad , \tag{2.30}$$

and the region around that point can be utilized to form a Gaussian model of the error using the technique in Section 2.2.2. If the center of the Gaussian error is outside the range contained within the mapping, it is simply wrapped into the range by a simple shift. One such estimation is illustrated in Fig. 2.7. The torque error, ε_T, given by Eq. 2.29, is modeled according to the process outlined in Eqs. 2.11-2.21.

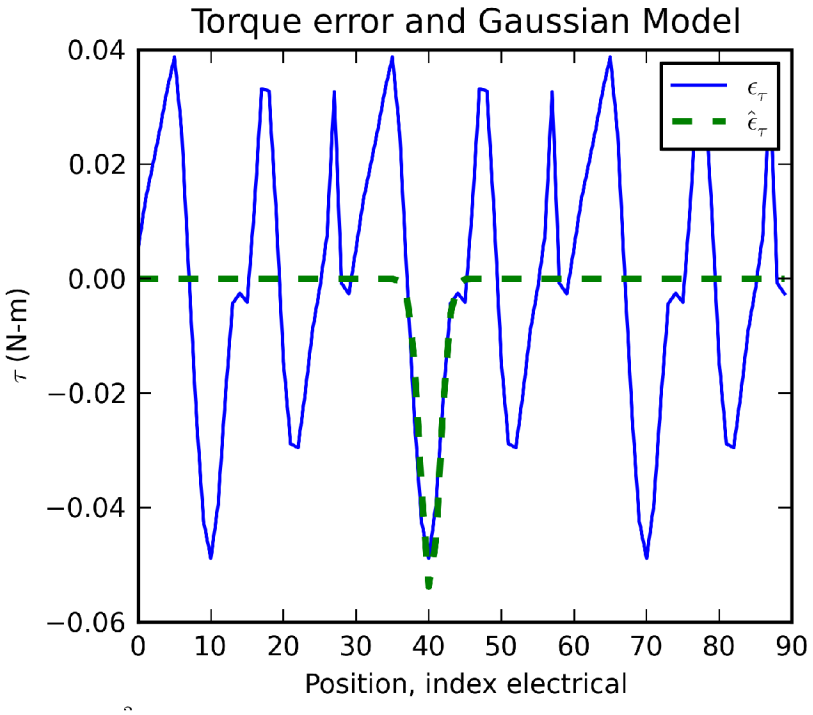

Fig. 2.7: Torque error and its Gaussian model.

Once the corrective signal is defined, the final step of the algorithm is to invert the mapping from rotor- to torque-perturbation (Eqs. 2.23-2.25) and arrive at a new rotor perturbation to be utilized in the next iteration of FEA simulation. This process is repeated until the torque ripple is below the desired threshold. For this instance, a torque ripple of <5% was desired. The progression of the gap function, phase torque, and other parameters are shown in Fig. 2.8.

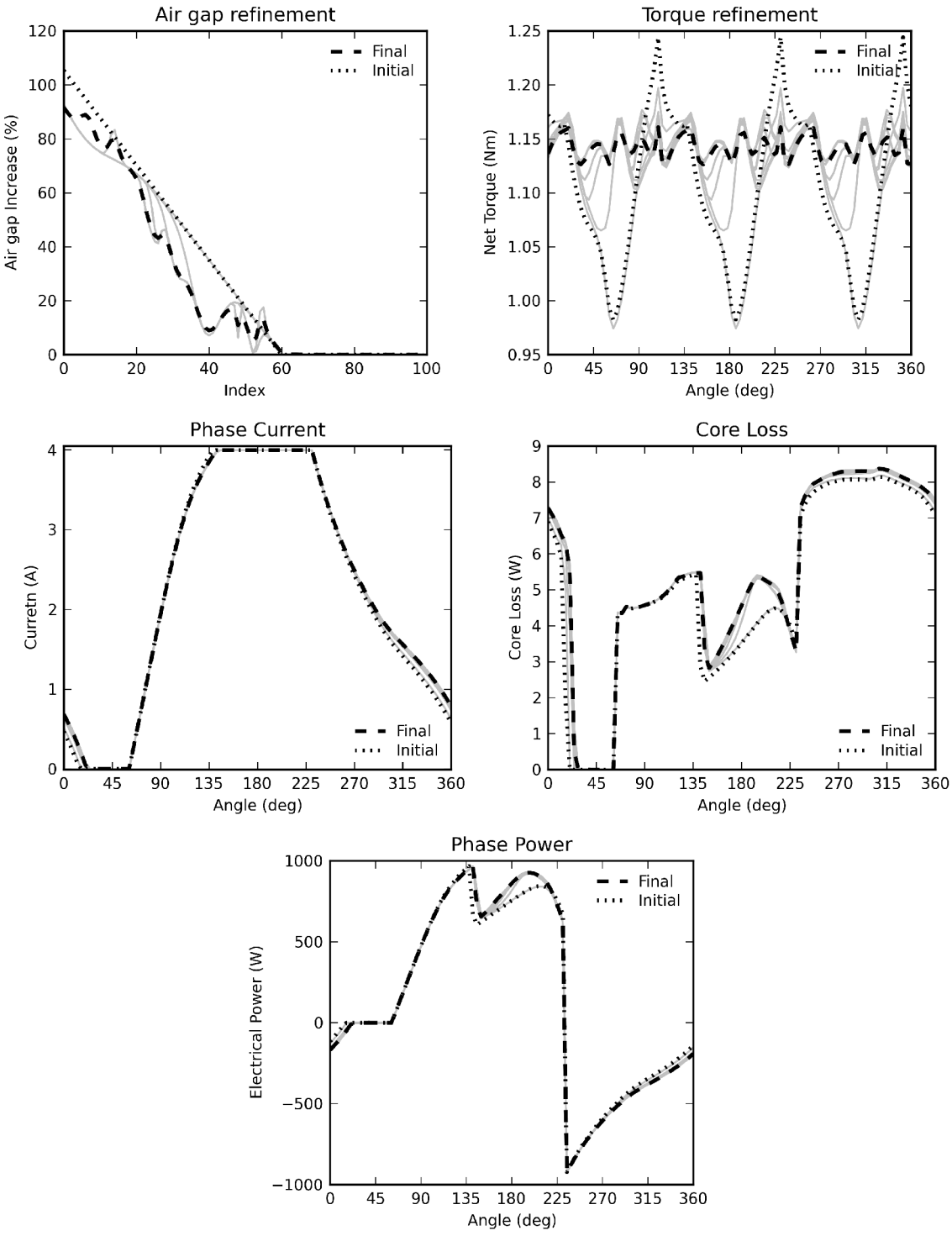

Fig. 2.8: Evolution of machine during refinement, clockwise from top left: gap function, torque, core loss, phase power, and phase current.

2.4 Summary

Using the inductance shaping algorithm, the peak-to-peak torque ripple was reduced from an initial value of 26.6% to 3.2% over nine iterations. The magnitudes of the torque ripple of each iteration are summarized in Table I. Table II lists the Gaussian parameters of the targeted portion of the torque ripple, the gap perturbation implemented to correct the target ripple, and the resultant torque perturbations due to the gap perturbation.

TABLE I FEA REFINEMENT OF TORQUE RIPPLE

Iteration	Average Torque (Nm)	Pk-pk ripple (%)
A	1.108	26.6
B	1.103	20.2
C	1.129	9.7
D	1.137	7.1
E	1.138	6.1
F	1.144	4.4
G	1.146	3.7
H	1.145	3.4
I	1.142	3.2

TABLE II TORQUE RIPPLE, ROTOR PERTURBATION, AND RESULTANT TORQUE PERTURBATION

Torque Error			Gap Perturbation			Resulting Torque Perturbations					
a	μ	σ	a	μ	σ	a	μ	σ	a	μ	σ
0.122	57.3	3.921	-0.050	10.0	3.000	0.006	33.7	4.926	-0.005	59.4	4.126
-0.125	46.0	3.988	-0.288	39.1	5.432	0.186	46.3	4.387	-0.050	75.7	5.816
-0.067	42.4	3.363	-0.175	31.0	3.117	0.068	42.6	3.141	-0.020	69.7	2.255
-0.046	40.0	1.962	0.050	25.7	1.595	-0.007	40.1	3.064	0.003	67.5	2.576
-0.035	51.8	2.400	-0.132	52.2	1.906	0.046	52.3	3.858	-0.010	79.9	5.827
-0.031	39.0	2.274	-0.129	23.3	1.695	0.020	38.9	3.818	-0.009	66.2	2.803
-0.036	50.1	0.864	-0.131	47.9	0.588	0.015	50.3	3.706	-0.004	79.5	4.484
0.029	53.2	1.538	0.131	54.5	1.049	-0.020	53.6	3.572	0.004	81.2	5.261
0.021	34.6	2.098	0.114	13.8	1.491	-0.010	34.5	3.652	0.006	61.2	3.813
0.023	47.4	0.982	0.118	62.8	0.628	-0.020	58.2	2.287	0.002	85.0	2.055
0.026	57.2	0.788	0.115	10.5	1.223	-0.006	33.6	4.408	0.005	59.5	3.831
0.019	57.3	1.200	0.105	17.3	3.894	-0.023	36.1	3.959	0.010	62.6	4.418

FEA was also performed on a conventional SRM machine with identical geometric parameters with the exception of a constant pole radius and minimum air gap. The magnitudes of the voltage and current utilized in the phase excitation were adjusted so that the net torque production was within 1% of the final iteration of the ShRM. Although rms phase current is slightly higher in the ShRM, core losses are much lower, thereby improving the overall efficiency of the machine. A summary of performance parameters for the SRM and final ShRM are provided in Table III.

TABLE III FEA REFINEMENT OF TORQUE RIPPLE

	SRM	ShRM	Difference
RMS phase current, A	2.61	2.70	3.5%
Average torque	1.136	1.1421	0.51%
Angular speed, RPM	3520	3520	0
Torque Ripple, %	56.1	3.2	17.5x
Core loss, W	23.1	18.2	-21.0%

These results show that the reduction of torque ripple can be accomplished strictly through the careful refinement of the machine geometry. Moreover, this reduction in torque ripple does not result in a machine with lower efficiency. The reduction of torque ripple accomplished without altering the phase excitation allows additional freedom in the implementation of the system controller. If desired, a much simpler control algorithm can be implemented, such as hysteresis control of phase current, and system costs can be lowered. It also allows the phase power to be modulated for other aims, such as reducing the system current and electrical power ripple, as seen in the next chapter.

Chapter 3: Excitation Shaping

In this section, the technique for refinement of the phase excitation is presented. The objective of the refinement is to drive the system electrical input power to a constant value at the operating point, regardless of rotor position, by balancing the energization and enervation of the phases.

Conventional design consists of simulating a machine at several dc phase currents, then constructing a look-up table to simulate the dynamic electrical response to a given phase excitation. This requires a large number of Finite Element Analysis (FEA) simulations for every iteration of the machine geometry. In order to accomplish this in a timely fashion, the electromagnetic properties of the machine are co-simulated with a simple driving circuit for each phase, whereby the phase is energized by a piece-wise continuous voltage or current waveform. After FEA completed, the voltage and current waveforms for each phase were collected and utilized to reconstruct the net machine electrical current and power, first by point-by-point multiplication to determine instantaneous phase power, then the phase powers were summed as follows:

$$P_e = \frac{1}{N} \sum_{n=0}^{N} i_n v_n \tag{3.1}$$

where N is the total number of phases, and i_n and v_n are the current and voltage in phase n.

The desired power waveform is the average power input without the ripple present in the simulation results,

$$P_e^* = \frac{1}{T}\int_{t=0}^{T} P_e \tag{3.2}$$

and the error term is simply the difference between the two:

$$\epsilon_{Pe} = P_e^* - P_e \tag{3.3}$$

This error signal is then masked and utilized to modify the excitation for the next iteration. The mask serves two purposes: (1) to confine the perturbation to a particular region of the excitation so that the phase does not develop current during the negative torque-producing region; (2) ensure that the perturbation of adjacent phases does not overlap and over-compensate in those areas.

The simplest mask is a simple rectangular window,

$$M[i] = \begin{cases} 0 & 0 \le i < i_m \\ 1 & i_m \le i < i_m + I/N \\ 0 & i_m + I/N \le i < I \end{cases} . \tag{3.4}$$

where I is the total number of samples in the signal, N is the number of phases in the machine, $\boldsymbol{i_m}$ is the index where the mask begins, and i is the index of the array. As an alternative, a continuous mask could be a two-way Gaussian step or trapezoidal, for example.

In the case of current-source excitation, the modification from step m to step $m+1$ is obtained by

$$i^{m+1} = i^m + k\, M \circ \epsilon_{Pe} \tag{3.5}$$

where

$$(x \circ y)[i] = x[i]\,y[i] \tag{3.6}$$

or a point-by-point multiplication, M is as described in Eq. 3.4, and k is a user-selected gain constant.

And for voltage excitation,

$$v_{m+1} = v_m + k\,M \circ \epsilon_{Pe} \tag{3.7}$$

One further modification was made to the voltage perturbation: if the perturbation created an imbalance between the maximum and minimum voltages, the voltage excitation was shifted to preserve the balance,

$$v_n = v_n - \frac{max(v_n) + min(v_n)}{2} \tag{3.8}$$

The effects of a voltage-source perturbation net electrical power, phase current, and phase torque are shown in Fig. 3.1.

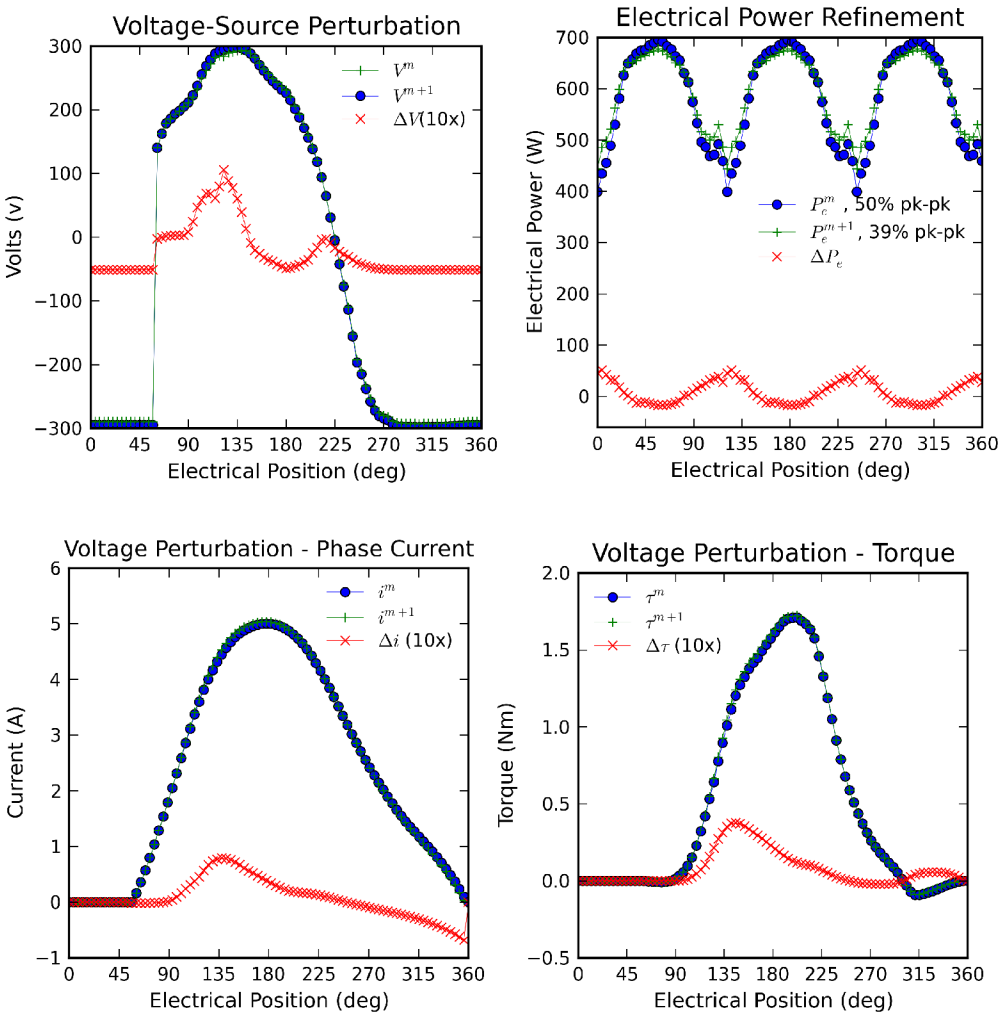

Fig. 3.1: The effects of perturbation of excitation voltage on other machine waveforms.

Chapter 4: DC Reluctance Machine Design

At this point, we have two perturbation methods: (1) geometry refinement to minimize torque ripple and (2) excitation refinement to minimize supply current. We have seen in previous chapters that a perturbation of one parameter set also has an effect on both torque and phase power. However, it is observed that geometric perturbations primarily affect torque, with less of an affect on electrical power. Similarly, phase excitation perturbations primarily affect electrical power and a more minor effect on torque. Therefore it is possible to target a specific region in the machine operation, be it mechanical or electrical, and minimize ripple in that region without severe and undesirable secondary effects.

4.1 Selection of Perturbation Mode

However, the separation of mechanical and electrical effects is not complete, making it difficult to attribute the change in response to a particular cause if both the machine geometry and excitation are changed. Therefore the mode of refinement must be selected at each iteration: either modification of the geometry or the phase excitation. The mode selection can be made according to a metric evaluating the property under consideration.

In this case, a simple and effective metric is the ratio of the peak-to-peak ripple to the average value of the wave form,

$$\beta(x)=\frac{max(x)-min(x)}{\bar{x}}, \tag{4.1}$$

and the mode is selected to target the highest β. In this fashion, the machine is refined to minimize ripple in both torque and input current.

4.2 Target Machine Specifications

In this fashion, the refinement method described in the previous chapters was applied to a machine simulated at steady-state operating conditions, with a constant output speed and voltage-source input. Under those assumptions, the mechanical power is directly proportional to the net machine torque and the electrical power is directly proportional to the supply current. The target machine was a ½ hp motor for household refrigerator compressor, a power level chosen for ease of prototyping and experimental studies. The envelope of the reference machine is described as the intersection of a 132mm diameter circle and a 109mm by 123mm rectangle, a stack height of 48mm and end turns of 20mm per side. This results in a total motor height of 88mm for a stack volume of approximately 630cm^3 and overall volume of 1160cm^3.

Ansys Maxwell 2D was utilized to evaluate a three-phase machine operating at a peak output of 1Nm and 3520rpm, or 368W. In this particular application, the machine sees the peak power on rare occasions, so the nominal operating condition was selected to be 0.81 Nm for an ouput power of 300W. The outer envelope was set by that of the reference machine and the minimum air gap was selected to be 0.25 mm, a comfortable margin above the minimum manufacturing tolerance of 0.20 mm. The proposed DCRM was chosen for a stack height of 30mm with a core volume of 312cm^3. End turns were projected to be 10mm per side, resulting in an overall volume of 520cm^3.

The initial air gap profile was the linear ramp described in Chapter 2 and the initial phase voltage was taken the simulation of the sinusoidal machine presented in [66]. The rotor speed was set at 3520rpm and FEA analysis produced the characteristics of the initial machine

geometry and excitation. The lamination design is shown in Fig. 4.1 and the key parameters of the geometry and operating condition are provided in Table IV.

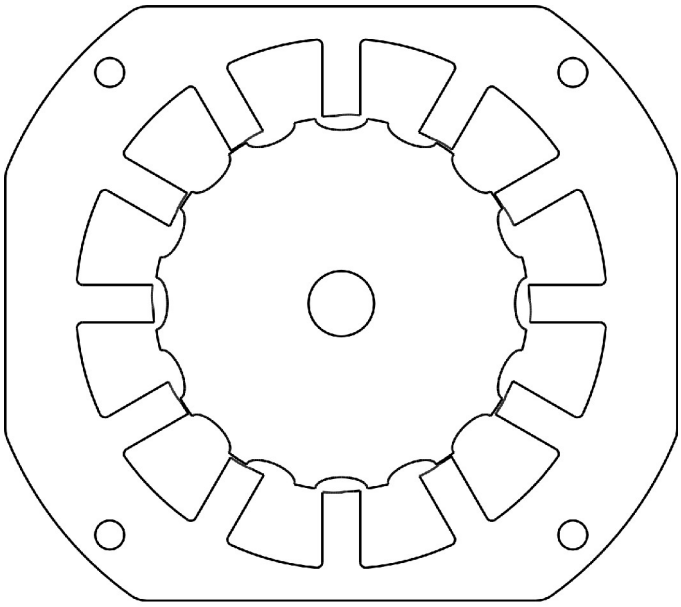

Fig. 4.1: Lamination design for 3-phase, 12/16 machine.

TABLE IV KEY MACHINE PARAMETERS

Phases, number	3
Reference Speed	3520 rpm
Reference Torque	0.81 Nm
Reference Power	300 W
Stator, max width	123mm
Stator, max OD	132mm
Stator, min width	109mm
Stack height	30mm
Air gap, min	0.25mm
Stator, min ID	69.0mm
Stator poles, number	12
Stator pole, arc	11.5º
Rotor, max OD	68.5mm
Rotor poles, number	16
Rotor pole, arc	6.5º

4.3 Design Refinement Process with FEA

Initial sizing of the machine was performed with conventional methods outlined in the literature of SRMs, *e.g.* making an effort to balance copper losses with core losses and selecting pole arcs to minimize torque ripple, which produced the geometric parameters for the interior of the machine listed in . The initial gap function was as described in Eq 2.5, which was a piece-wise linear ramp with one region being a constant zero. The initial phase voltage excitation was the result of a study evaluating the feasibility of producing the machine described in [5], which is presented in [66]. With these parameters as the starting point, the perturbation refinement algorithms proposed in this dissertation were applied.

Fig. 4.2 shows the initial electrical and mechanical power wave forms, where the individual phase contribution is shown as a dashed red line and the net quantity is shown as solid blue. The electrical power had a peak-to-peak ripple of three times its average, while the peak-to-peak mechanical power ripple was almost equal to the average mechanical power. Assuming a constant voltage source, the ripple in electrical power electrical will manifest in a proportional ripple in the converter current. Conversely, the ripple in the mechanical power translates to ripple in the net machine torque from the system at constant angular velocity. The refinement algorithm, utilizing the techniques described in Chapters 3 and 4, improves the phase excitation and inductance profiles through successive iterations and reduces the variations in converter and mechanical power to their final values Fig. 4.3. The progression of power ripple improvements are summarized in Table V. Fig. 4.4 shows the final air gap of the DCRM (operating with shaped

phase current), in contrast to that of the ShRM (operating with trapezoidal phase current) from Chapter 2.

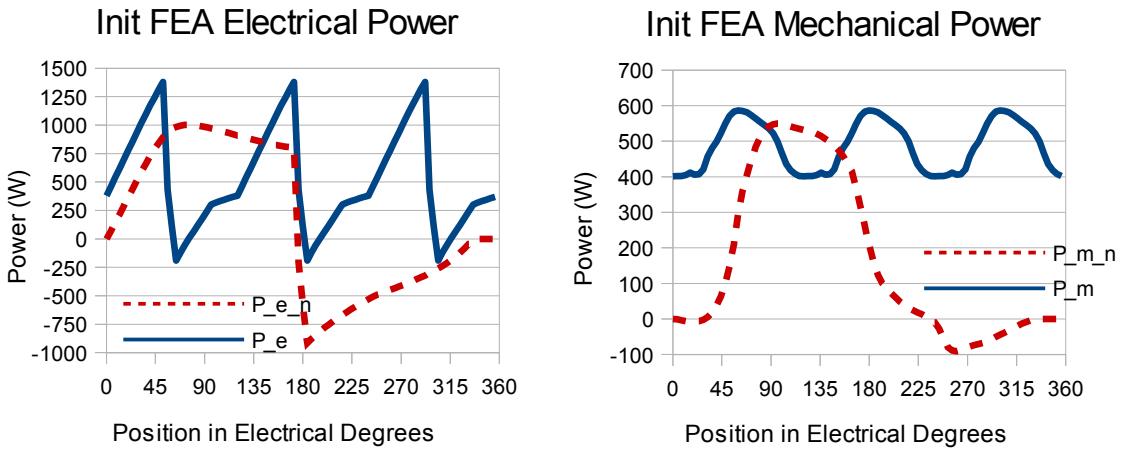

Fig. 4.2: Initial electrical (top) and mechanical (bottom) power wave forms for a conventional three-phase SRM.

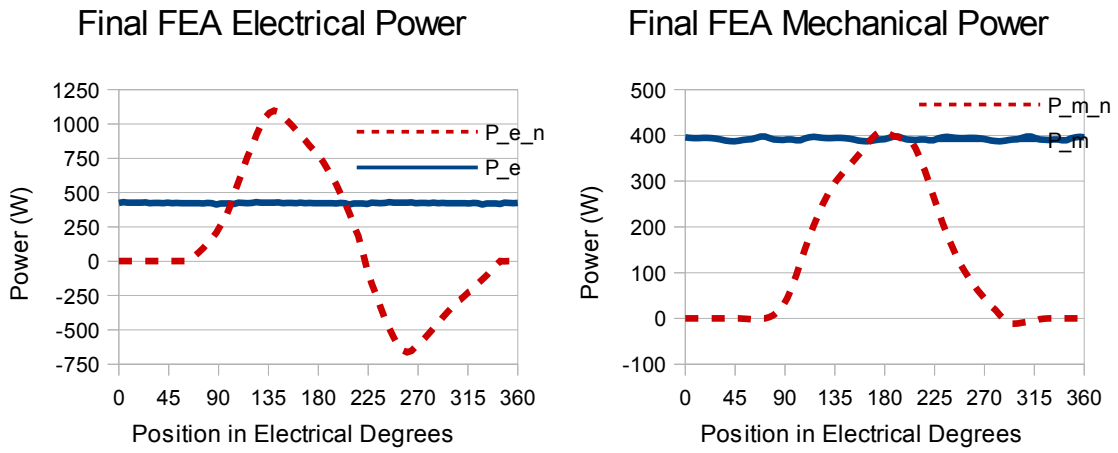

Fig. 4.3: Final electrical (left) and mechanical (right) power wave forms for a three-phase DCRM.

TABLE V FEA REFINEMENT OF POWER RIPPLE

Iteration	% Electrical Ripple	% Mech. Ripple
A	308	38.1
B	84.9	17.4
C	80.7	13
D	42.89	9.69
E	8.33	7.18
F	6.45	2.89
G	4.41	2.64

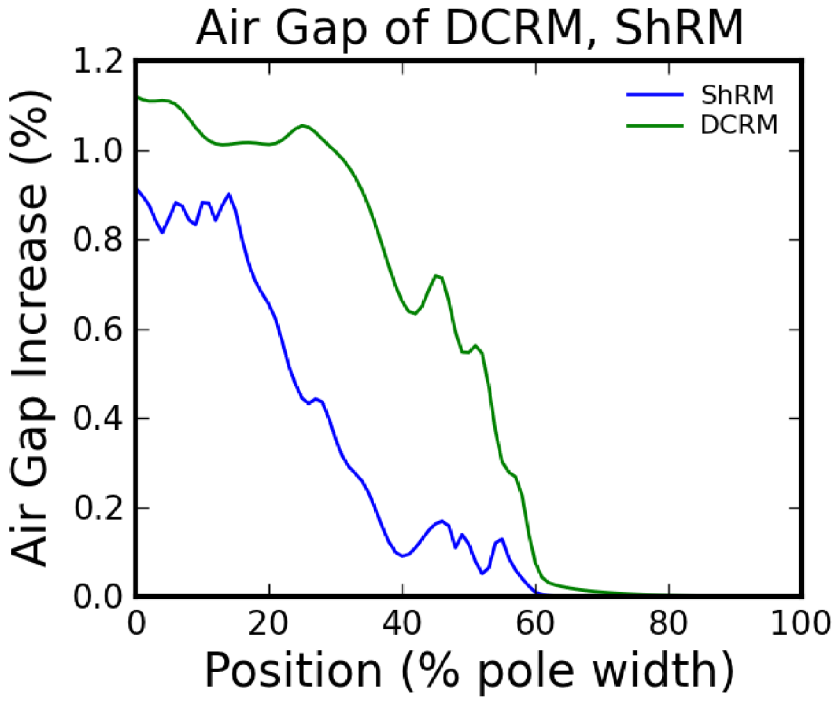

Fig. 4.4: Air gap of DCR, in relation to that of the ShRM in Chapter 3.

4.4 Comparison to Conventional SRM

FEA was also performed on a SRM with flat poles and conventional hysteresis-controlled phase currents, with the same geometric properties as the DCRM. The setpoint for the hysteresis current controller was adjusted to obtain an average torque within 1% of the DCRM. Although the phase current in the conventional SRM is lower than that of the DCRM, the overall efficiency of the DCRM is favorable due to a reduction in the core losses of the machine. A full comparison of operational parameters is made in Table VI.

TABLE VI SRM AND DCRM COMPARISON

Quantity	SRM	DCRM	Difference
Speed (rpm)	3520	3520	~
Avg. Torque (Nm)	0.842	0.841	-0.1%
Stator Envelope (mm)	109x123	109x123	~
Stator ID (mm)	69	69	~
Air Gap (mm)	0.25	0.25	~
Stack Height (mm)	30	30	~
Torque Ripple, pk-pk (%)	50.2	2.64	19x
Input Current Ripple, pk-pk (%)	377	4.41	85x
Phase current (A_{RMS})	5.89	5.91	0.3%
Core Losses (W/%)	18.2/6.1%	12.6/4.2%	-44%
Copper Losses (W/%)	31.2/10.4%	31.4/10.5%	0.6%
Efficiency (%)	83.5%	85.3%	+1.8%

4.5 Summary

With the smaller stack height and the concentrated windings, the DCRM has a large reduction in volume over the reference machine. The refinement algorithm successfully reduced the peak-to-peak ripple of the electrical power to less than 5% and the mechanical power ripple to less than 3%. As the design process was carried out under the assumption of a constant voltage input to the system and constant mechanical speed, this` corresponds to less than 5% current ripple from the supply and 3% torque ripple. Effectively, the process produces a doubly-salient reluctance machine which appears as a dc source and sink, a DCRM.

When compared to conventional DSRM design and control, the SRM has 85 times more source current ripple and 19 times more torque ripple. Although phase current is slightly higher in the DCRM, core losses are lower, maintaining efficiency. This design study shows that a DCRM is not only feasible, it retains efficiency and enables a substantial reduction in volume over existing technology.

Chapter 5: Experimental Results

A prototype machine was constructed and assembled, shown in Fig. 5.1. The machine was tested in both static and dynamic conditions. Static tests consist of locked-rotor torque and inductance measurements versus position, while the dynamic tests were performed with the machine rotating under its own power against a load in steady state. Both of these tests are commonly performed for RMs to validate the FEA model.

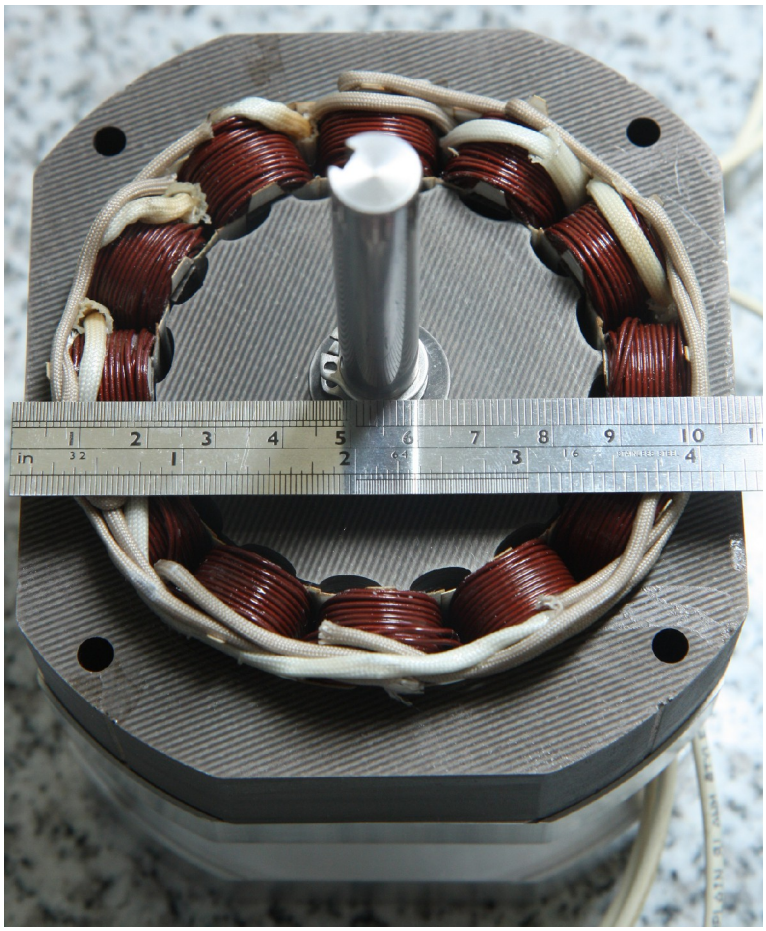

Fig. 5.1: The prototype machine.

5.1 Static Tests

Static torque tests generously performed by Whirlpool Corporation, in which a single phase is energized with a constant current for the entire electrical cycle. These tests revealed that the experimental data did not match the FEA of the target design, with an additional 20% current needed to obtain the desired torque point. Subsequent FEA studies have shown that increasing the air gap from 0.25mm to 0.47mm shows good correlation with the experimental data at all current levels (Fig. 5.2).

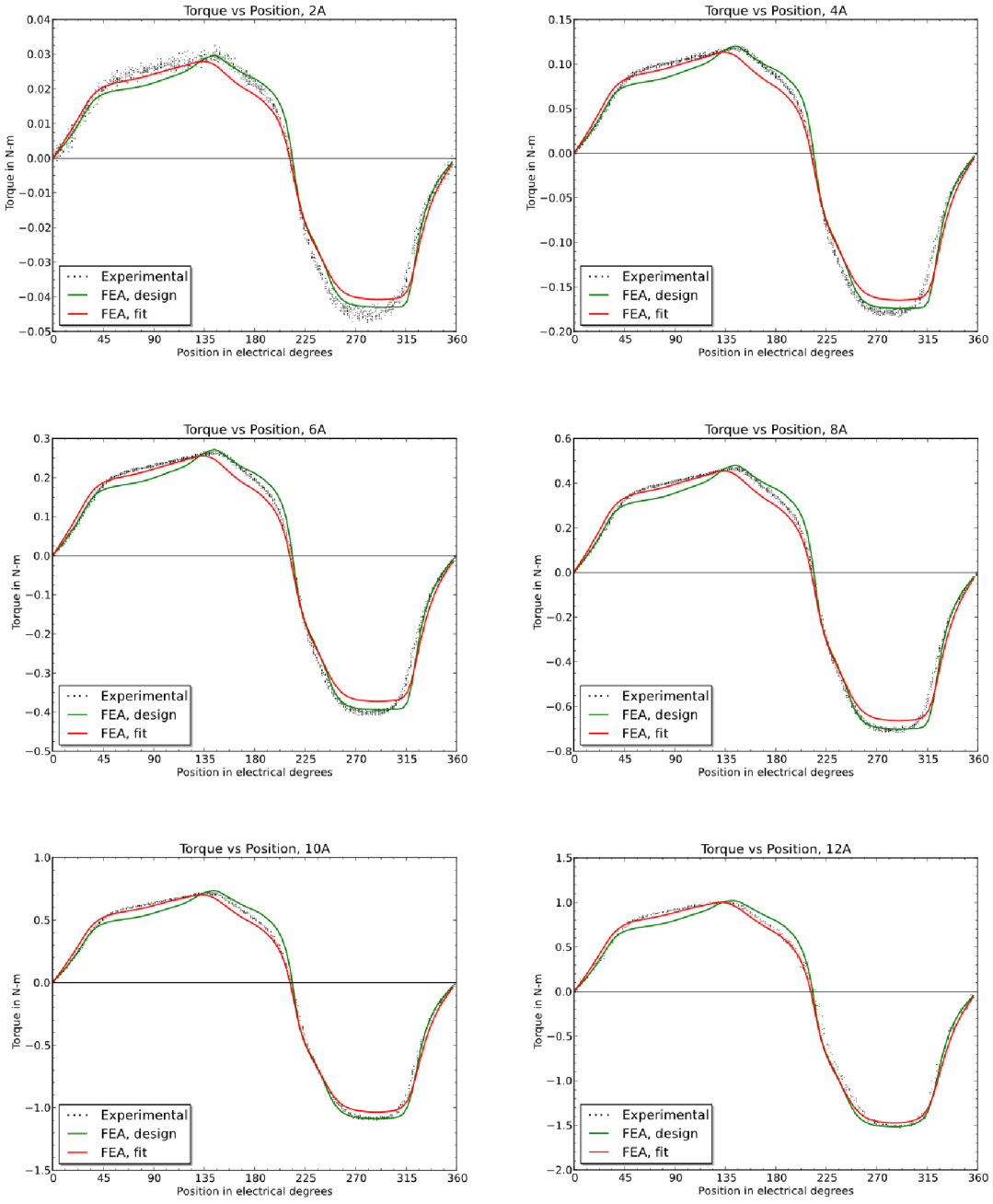

Fig. 5.2: Experimental vs modeled static torque waveforms at various currents.

While disappointing, the correlation between the modified FEA model and the experimental data indicates that an error occurred during manufacturing or assembly of the prototype machine.

One confirmed defect was a warping of the shaft, which was resulted from interior stress relief during machining of the shaft. Such a warping produces in an eccentricity between the rotor and stator which varies from one lamination to the next. The shaft was re-manufactured, but static torque tests were not performed for the replacement shaft. Inductance measurements were made with the replacement shaft and are shown in Fig. 5.3.

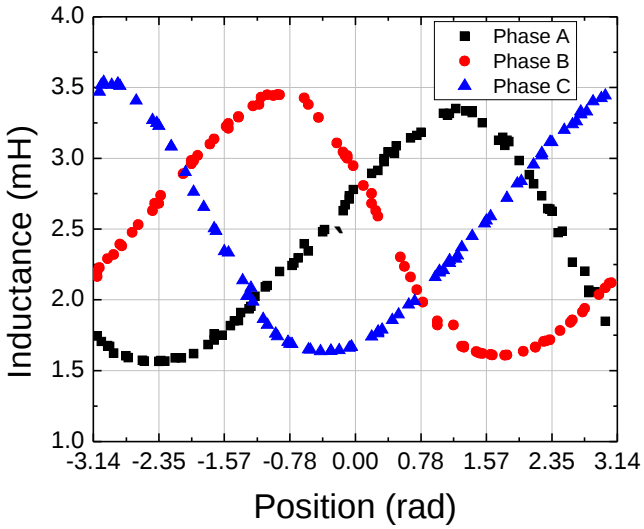

Fig. 5.3: Phase inductance measurements for the prototype machine.

Based on the static torque tests, which are conducted at a constant current for all positions, the torque waveforms of the prototype were calculated utilizing the phase current profile from the final iteration in Chapter 4 (Fig. 5.4). To interpolate for values of current between the samples in Fig. 5.2, the torque was computed as

$$T\left(\theta, i_{ref}\right)=\left(1-\gamma\right)T\left(\theta, i_1\right)+\gamma\, T\left(\theta, i_2\right). \tag{5.1}$$

where γ is computed as

$$\gamma=\frac{i_{ref}^2-i_1^2}{i_2^2-i_1^2}, \tag{5.2}$$

where i_{ref} is the reference current shown on the left side of Fig. 5.4, and i_1 and i_2 are the bounding currents from Fig. 5.2. In this fashion the ripple component of the net machine torque was calculated to be 9.54%, an improvement of 5 times compared to conventional DSRM practice, in spite of the discrepancy between the prototype and the FEA model.

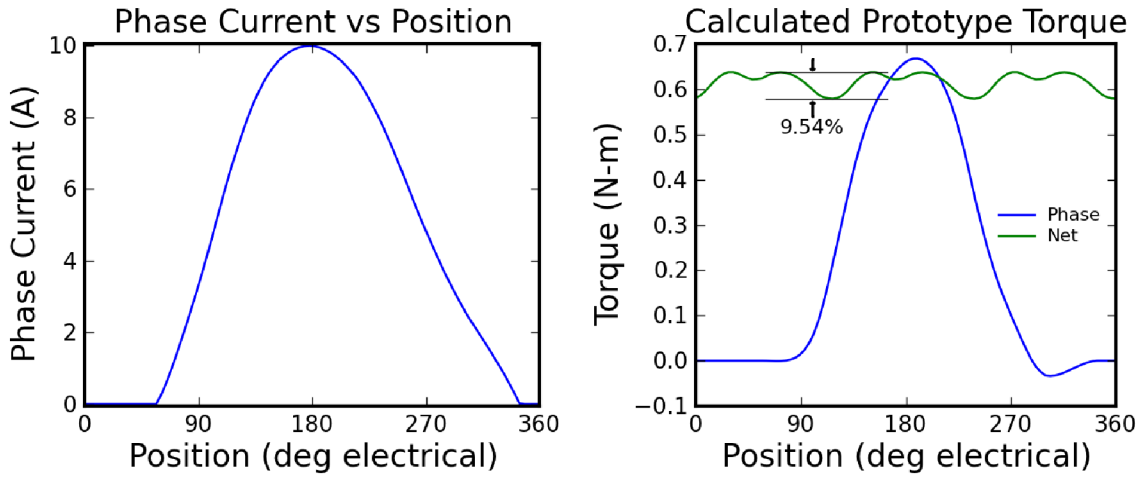

Fig. 5.4: Using the final current profile from the FEA refinement process (left), the per-phase and net torque (right) are calculated based on the static torque waveforms .

5.2 Dynamic Tests

Dynamic results were also conducted for the machine utilizing dynamometer setup shown in Fig. 5.5. Torque was measured with a Himmelstein MCRT48291, rated at 25 lbf-in (2.8Nm), and the phase electrical characteristics were measured using a Yokogawa WT1600 3-channel digital power meter. Load was provided by an Anaheim Automation BLY344D, which is a trapezoidal BLDC machine, connected to a current-controlled load through a three-phase full-bridge rectifier. Power was provided by a 150VDC source with a 24μH/10μF low-pass input filter to damp harmonics of the pulse-width modulation carrier frequency. System control and data acquisition was performed over RS-232 and collected through a graphical user interface written in Python. Traces of the analog torque transducer output and the voltage of the 10μF capacitor on the drive board were made with passive oscilloscope probes and the source current was measured with a LeCroy AP015 active current probe rated at 30A, 50MHz. A conventional asymmetric half-bridge converter was utilized to drive the machine (Fig. 5.6).

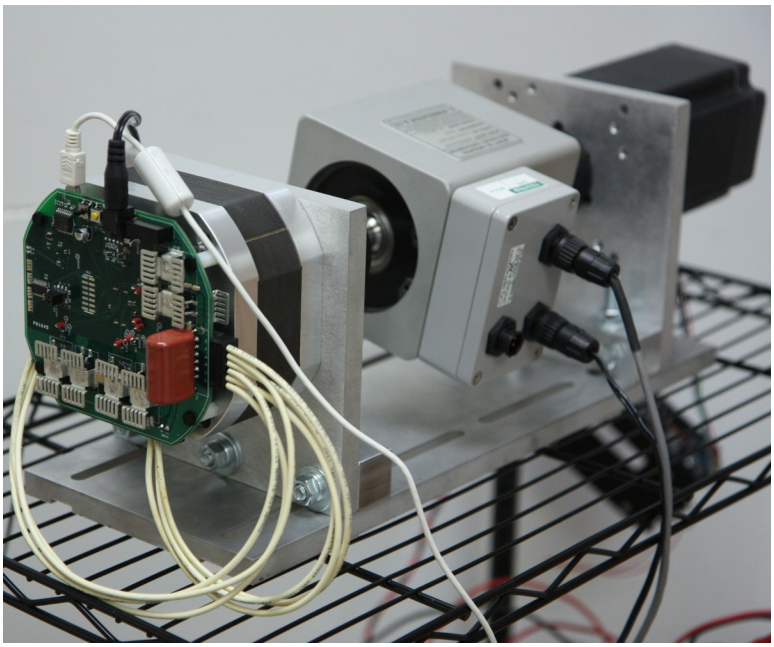

Fig. 5.5: Dynamometer setup for dynamic testing of prototype DCRM.

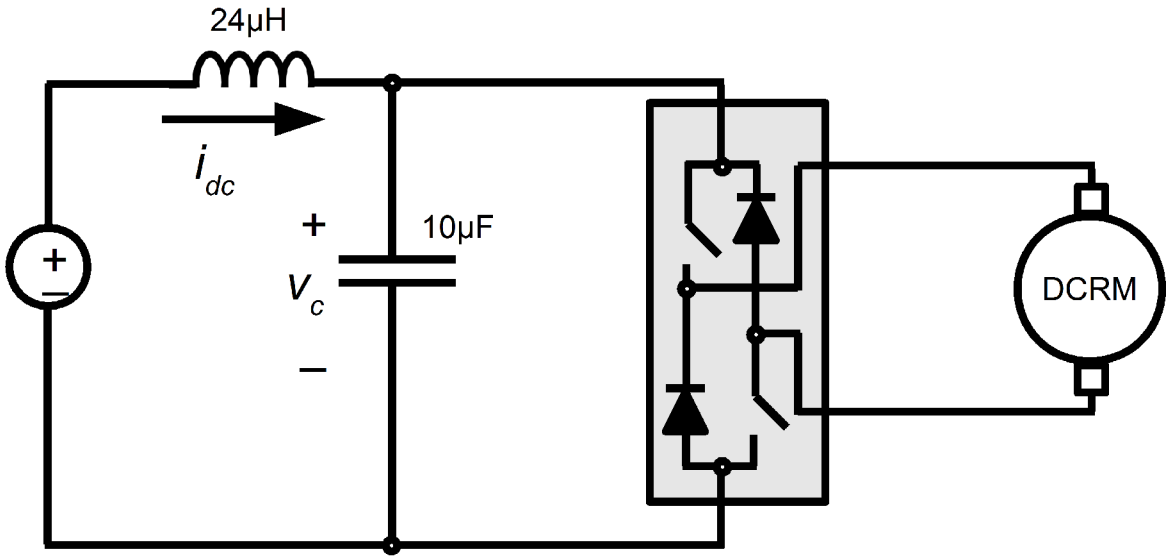

Fig. 5.6: The DCRM is driven by a conventional asymmetric half-bridge converter and connected to the DC voltage source through an LC low-pass filter.

For the purposes of design verification, the phase excitation was done in an open-loop fashion with a TMS320F28069 microcontroller from Texas Instruments. The phase voltage as a

function of rotor position was taken from the final iteration in Chapter 4 was programmed into the system controller as a look-up table (LUT). A PI speed controller was implemented to maintain a set speed, ω. The voltage was applied to the machine windings through Pulse-Width Modulation (PWM), where the carrier frequency was 30kHz. A block diagram on the system controller is shown in Fig. 5.7.

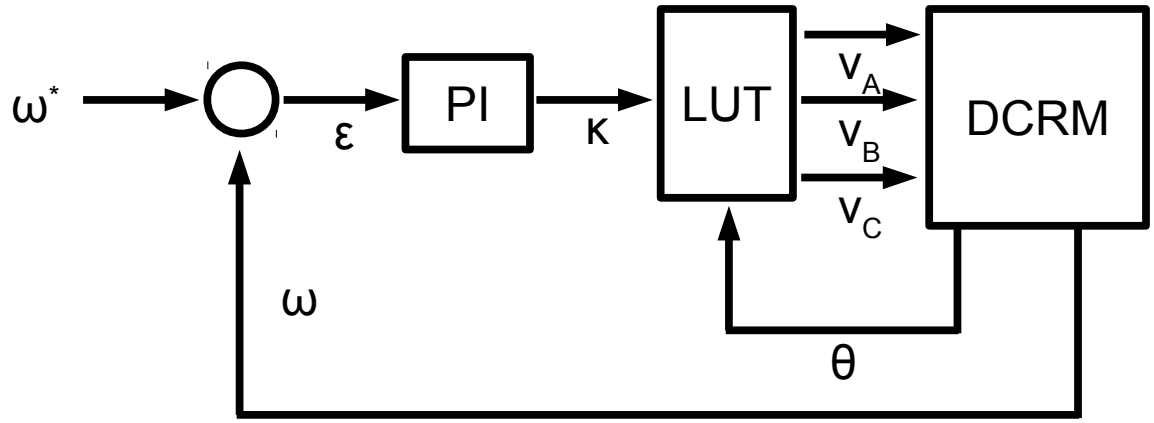

Fig. 5.7: Block diagram of DCRM controller.

During testing, it was evident from oscilloscope that several harmonics, in addition to harmonics of the phase frequency, were present in the traces representing torque, source voltage, and source current, both lower frequency (e.g. speed control loop) and higher (e.g. pulse-width modulation). The raw data points were saved (1.2M-samples per channel) and are shown in Fig. 5.8, the FFT of the raw signals are shown in Fig. 5.9.

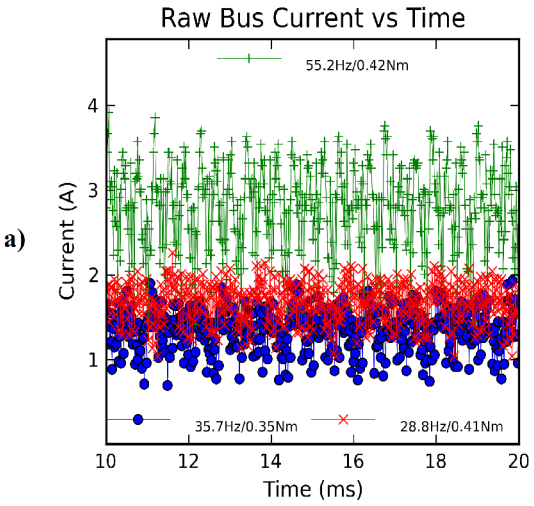

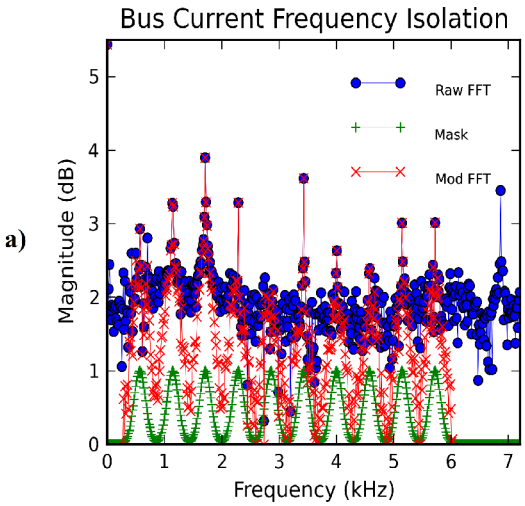

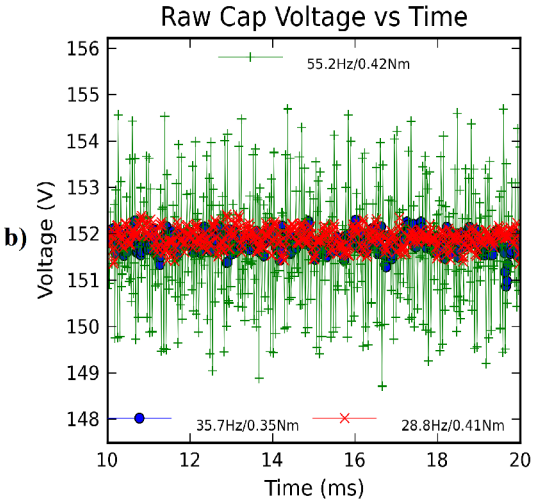

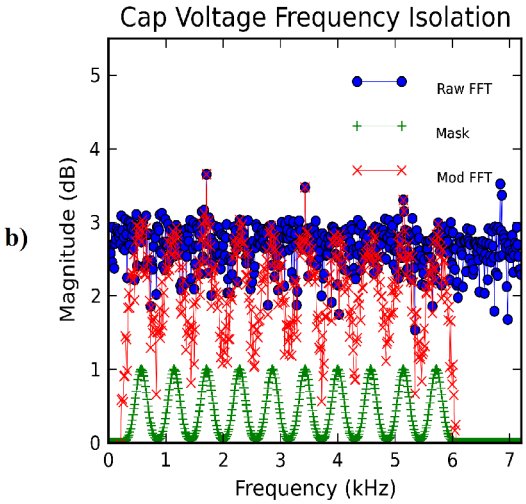

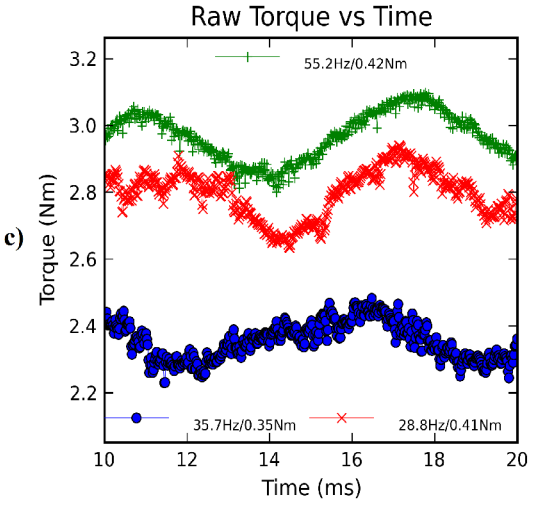

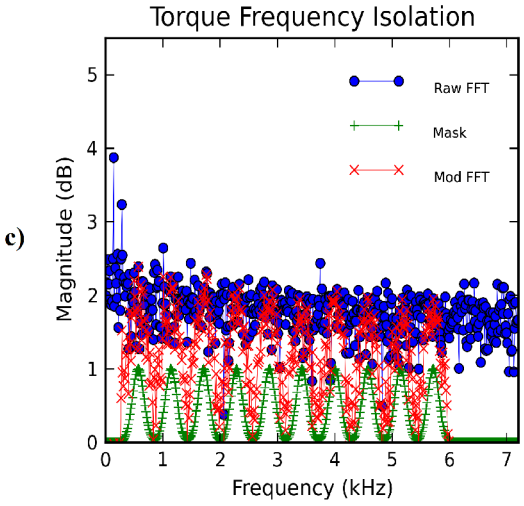

Fig. 5.8: Raw experimental waveforms for 3 load ***Fig. 5.9: Isolation of the phase frequency***

In order to isolate the effects of the design process, the frequency content of the signals were masked to contain the DC component and the first ten harmonics of the electrical phase frequency. This was accomplished by applying a mask to the FFT of the raw signal,

$$M = \sum_{n=1}^{10} \exp\left(\frac{-\left(\omega - n\,\omega_0 \right)^2}{\sigma^2} \right), \tag{5.3}$$

and the resulting filtered wave forms are plotted in Fig. 5.10, where ω_0 is the phase frequency, and σ is the bandwidth of the filter.

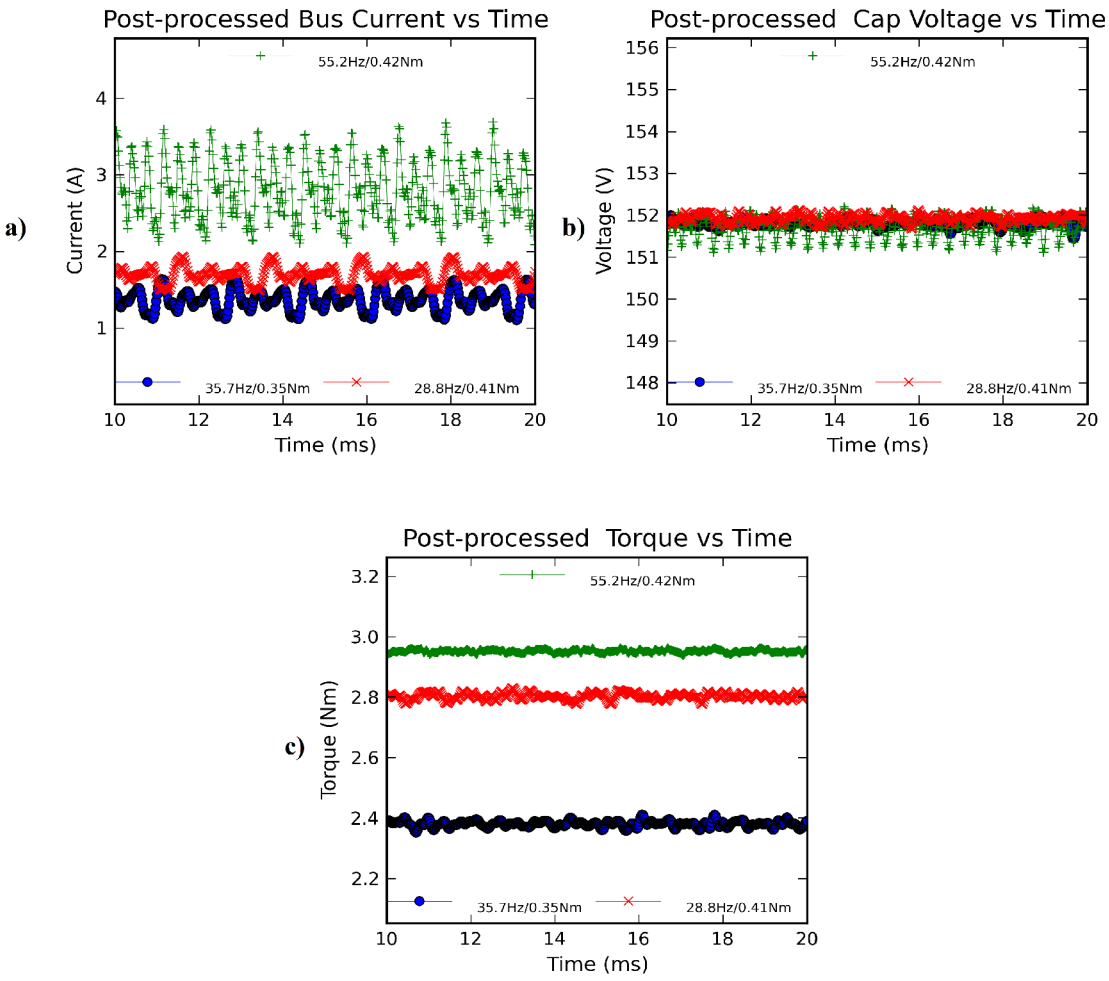

Fig. 5.10: Filtered experimental waveforms for 3 load points.

The energy of the ripple contained in the harmonics of the phase frequency was calculated as

$$\beta_{ripp}(x)=\frac{RMS(x-\bar{x})}{\bar{x}}. \qquad (5.4)$$

and are listed in Table VII for three operating points. Current and voltage waveforms have some harmonic content, less than 15% and 0.2%, respectively, which is much reduced compared to conventional implementations. The torque feedback has very low harmonic content, <0.5%, but

it is limited by the frequency response (200Hz) of the transducer and mechanical system. These results show the effectiveness of the DCRM design process at improving the ripple content of the electrical and mechanical power spectra, in spite of the discrepancy between the model and the prototype machine.

TABLE VII POWER RIPPLE, EXPERIMENTAL TESTS

Input Filter	24μH/10μF		
Torque (Nm)	0.79	0.67	0.83
Speed (rpm)	1729	2144	3311
Output Power (W)	143	151	289
Torque, β_{ripp} (%)	0.35	0.48	0.36
Current, βripp (%)*	6.3	9.9	13.6
Voltage, βripp (%)	0.06	0.07	0.16

* For the filtered harmonic waveforms

Finally, the efficiency map of the system is illustrated in Fig. 5.11 and listed in Table VIII and Table IX for various load points. It is noted that the system efficiency at the rated point is lower than that of the FEA model. The rms current of the phases was noted during operation and the phase resistance has been measured at operating temperature. From this data, the copper losses are calculated to be 46.6W (14.9%) and core losses are 23.4W (7.5%). Both of these quantities are much higher than those in the target FEA model, which can be related to the deviation of the static torque profile from the FEA model. However, it is noted that the prototype can be directly compared to a design in literature [23]. The prototype is competitive in efficiency

at the listed load point, although with a stack height that is shorter by 6mm (18%). In this work, the measured efficiency was 70.5% at 1618 rpm and 0.234Nm (39.7W), whereas the prototype measured 69.4% efficiency at 1380 rpm and 0.299 Nm (62.4W).

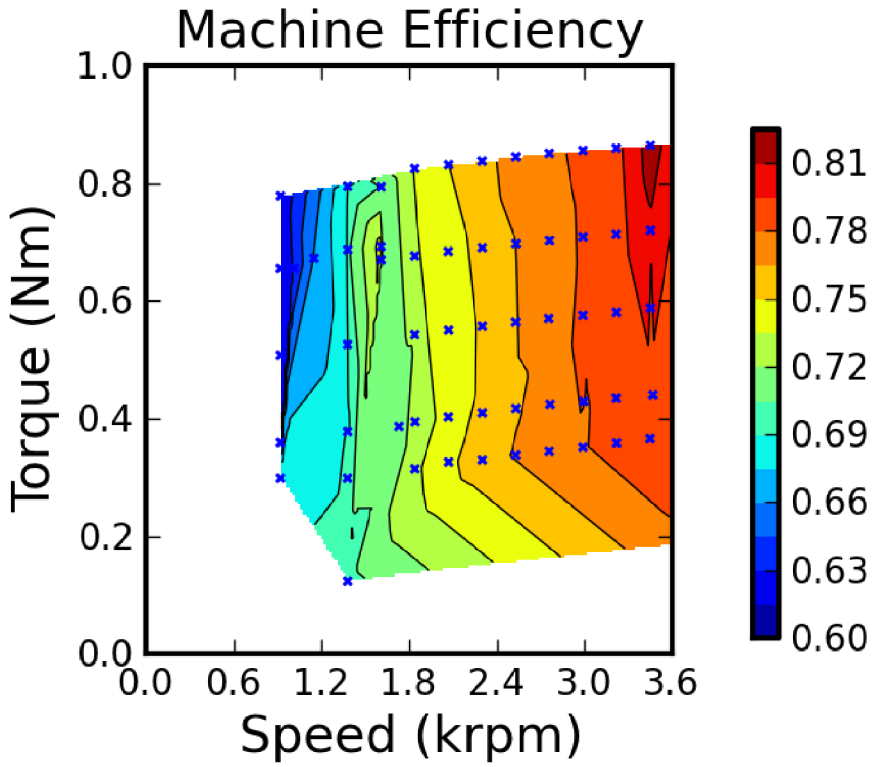

Fig. 5.11: Machine efficiency at various load points

TABLE VIII EXPERIMENTAL TEST MEASUREMENTS, PART I

Set Speed	MCU Speed	Torque	Mechanical Power	Phase Electrical Power			Mach. Elec. Power	Machine Efficiency
ω* (RPM)	ω (RPM)	T (N-m)	P (W)	P_A (W)	P_B (W)	P_C (W)	P_Σ (W)	(%)
1000	997.8	0.6553	63.12	37.1	32.8	32.9	102.8	61.40
1100	1101.2	0.6555	69.4	39.7	35.1	35	109.8	63.21
1250	1249.4	0.6728	80.9	44.3	39.1	39	122.4	66.09
1500	1501.3	0.6871	99.2	51.3	45.3	44.6	141.2	70.25
1750	1746.5	0.6926	116.8	57.2	50.6	49.8	157.6	74.11
1750	1751.3	0.6700	112.8	56.7	50.6	49.5	156.8	71.94
2000	2000.1	0.6766	130.3	64.5	57.5	56	178	73.20
2250	2249.4	0.6843	148.2	72.3	64.1	62	198.4	74.70
2500	2503.4	0.6907	166.23	79.6	71	68.5	219.1	75.87
2750	2749.2	0.6975	184.5	87.4	77.7	75.1	240.2	76.81
3000	3000.5	0.7030	202.8	95.4	85	81.5	261.9	77.43
3250	3248.5	0.7090	221.9	103.5	91.9	88.2	283.6	78.24
3500	3498.0	0.7133	240.6	111.2	98.9	94.6	304.7	78.96
3750	3754.7	0.7203	260.1	119.8	106.3	101.4	327.5	79.42
4000	3997.8	0.7265	279.9	128.8	114.1	108.6	351.5	79.63
1000	1001.0	0.7788	75	43.6	39	38.9	121.5	61.73
1500	1498.7	0.7950	114.8	60.1	53.7	52.7	166.5	68.95
1750	1748.6	0.7941	133.9	69	60.8	59.9	189.7	70.59
2000	2000.1	0.8254	158.8	78.6	69.3	67.8	215.7	73.62
2250	2252.0	0.8318	180.2	87.5	77.4	75.4	240.3	74.99
2500	2499.2	0.8380	201.9	96.7	85.5	83.1	265.3	76.10
2750	2749.9	0.8451	223.7	106.2	93.4	90.8	290.4	77.03
3000	2999.3	0.8510	245.7	115.6	102.2	98.5	316.3	77.68
3250	3250.7	0.8559	267.4	124.9	110.3	106.2	341.4	78.32
3500	3498.0	0.8598	289.5	134.2	118.6	113.6	366.4	79.01

TABLE IX EXPERIMENTAL TEST MEASUREMENTS, PART II

Set Speed	MCU Speed	Torque	Mechanical Power	Phase Electrical Power			Mach. Elec. Power	Machine Efficiency
ω* (RPM)	ω (RPM)	T (N-m)	P (W)	P_A (W)	P_B (W)	P_C (W)	P_Σ (W)	(%)
2250	2252.0	0.5504	119.3	58.6	52.4	51	162	73.64
2500	2500.5	0.5570	134.5	64.7	57.9	56	178.6	75.31
2750	2747.2	0.5640	149.3	71.4	63.6	61.5	196.5	75.98
3000	2996.8	0.5702	164.7	78.1	69.6	66.9	214.6	76.75
3250	3254.9	0.5757	182	84.4	75.1	72.2	231.7	78.55
3500	3499.9	0.5807	195.7	91.2	81	77.6	249.8	78.34
3750	3752.6	0.5880	211.6	98.1	86.9	83.3	268.3	78.87
4000	3997.8	0.5911	227.5	104.9	93.2	89.1	287.2	79.21
1000	1000.3	0.3591	34.6	20.1	18.1	18.2	56.4	61.35
1500	1499.0	0.3776	54.57	28.6	25.6	25.3	79.5	68.64
1750	1881.9	0.3864	65.15	33.1	29.5	29.2	91.8	70.97
2000	1861.7	0.3945	75.95	37.9	33.7	33	104.6	72.61
2250	2247.1	0.4028	87.3	42.7	38	37.2	117.9	74.05
2500	2502.7	0.4098	98.57	47.5	42.2	41.1	130.8	75.36
2750	2749.2	0.4171	110.39	52.4	46.7	45.5	144.6	76.34
3005	3004.4	0.4243	122.7	58.1	51.6	49.9	159.6	76.88
3250	3256.2	0.4293	134.4	62.9	55.8	53.8	172.5	77.91
3500	3491.0	0.4346	146.37	68.1	60.4	58.1	186.6	78.44
3750	3772.9	0.4403	159.05	73.7	65	62.6	201.3	79.01
4000	3978.5	0.4480	171.4	79.1	70	67	216.1	79.32
4000	3995.4	0.3725	143.4	66.6	58.8	56.3	181.7	78.92
3750	3753.1	0.3657	131.9	61.4	54.2	52.2	167.8	78.61
3500	3502.0	0.3582	120.7	56.3	49.7	48	154	78.38
3250	3248.8	0.3510	109.8	51.4	45.4	44.1	140.9	77.93
3000	2998.7	0.3446	99.53	46.9	41.5	40.2	128.6	77.40
2750	2749.9	0.3378	89.5	42.5	37.6	36.7	116.8	76.63
2500	2502.6	0.3297	79.35	38	33.6	32.9	104.5	75.93
2250	2249.5	0.3260	69.95	34	30.1	29.6	93.7	74.65
2000	1999.5	0.3145	60.55	30.1	26.5	26.1	82.7	73.22
1500	1498.9	0.2985	43.11	22.4	19.9	19.8	62.1	69.42
1000	1001.1	0.2985	28.77	15.2	13.4	13.7	42.3	68.01
1500	1500.0	0.1232	17.8	9.3	8	8.1	25.4	70.08
4000	4001.5	0.1875	72.15	34.1	29.8	28.8	92.7	77.83

Chapter 6: Conclusions

6.1 Summary

In this dissertation, methods have been proposed for reducing torque ripple and source current ripple in Doubly-Salient Reluctance Machines (DSRMs) to produce a DC Reluctance Machine, or DCRM. The need for such a machine has been cited by industry and academia, but approaches up to this point have taken a reductionist approach, considering only machine geometry or excitation strategy, only torque ripple or dc link current ripple.

The perturbation method proposed in Chapter 2 demonstrated that, for a given excitation, torque ripple could be controlled by manipulation of the radius of the pole face. It was also found that, in controlling torque ripple, machine efficiency was not adversely impacted, as an increase in copper loss was offset by a decrease in core losses. The resulting machine is termed Shaped RM (ShRM), as the manipulation of the pole face shapes the reluctance of the magnetic circuit to allow for low ripple torque production, less than 5% in the included design study.

Chapter 3 presented a perturbation method for reducing ripple in the net electrical power and current of the machine. This method is suitable for use with FEA tools to speed simulation time, as the drive circuit is co-simulated with the electromagnetic structure. This co-simulation is key to enabling the design of a machine with controlled electrical and mechanical power ripple.

Chapter 4 integrated these approaches in a design process to produce a DC Reluctance Machine, or DCRM. By alternating perturbation modes between geometric and excitation, an iterative approach demonstrated reduction of power ripple to negligible levels, less than 5% peak-to-peak ripple for input current and less than 3% peak-to-peak ripple for the torque. The final product compared favorably to conventional Doubly-Salient Reluctance Machine design and excitation, whereby electrical power ripple is reduced by 85 times and torque ripple is reduced by 19 times.

A physical prototype of the machine was constructed and its performance was noted in Chapter 5. Although the static torque profile of the prototype machine did not match the desired model, a modification to the model was identified that was in good agreement with the experimental data, leading credence to the supposition that the prototype geometry differed from the desired model. Even so, the net machine torque was calculated to have a ripple of less than 10%, 5 times better than conventional practice. Subsequent dynamic tests demonstrated that input current did, in fact, have very low ripple (<15%) and the torque ripple was not measurable (<0.5%). Peak machine efficiency was measured at 81.6%. The prototype machine efficiency is comparable to a similar design reported in literature, albeit with an 18% (6mm) smaller stack height.

The successful design, model, construction, and testing of a DCRM challenges basic presumptions about the capabilities of Doubly-Salient Reluctance Machines, in that they need not embody large ripple torque, nor do they require a large bank of electrolytic capacitors to absorb and emit power to the phase windings during commutation.

6.2 Contributions

The contributions of this work have been:

- proposed and implemented algorithm for eliminating torque and mechanical ripple by controlling the machine geometry, producing a Shaped Reluctance Machine (ShRM);
- proposed and implemented algorithm for eliminating converter current and electrical power ripple in the machine design phase by modifying phase excitation waveform;
- integrated the above algorithms to design a doubly-salient reluctance machine with very low ripple in both electrical and mechanical power at the design point, a DC Reluctance Machine (DCRM);
- constructed and tested prototype DCRM, confirming design goals and algorithms.

6.3 Future Work

In addition to these contributions, there is further work to be performed to realize the full system potential and speed the design process. Further work remains to be performed on the design algorithms, analysis over a broader operating range, and optimize system control under unforeseen conditions.

From the design standpoint, it is noted that the final pole geometry and its associated gap function appears jagged and does not increase monotonically. Moreover, the correlation between the parameters of the gap function perturbation and the torque waveform perturbation is not ideal. A more comprehensive understanding of the relationship between gap function and the machine torque characteristic could improve the correlation of parameters and produce a more aesthetically pleasing gap function while improving the speed of convergence of the torque refinement algorithm.

On the side of electrical power ripple, it is noted that the phase excitation assumed a triangular waveform. Other shapes of power waveforms may be possible that offer more desirable characteristics, such as lowering conduction losses within the machine or reducing peak voltage or current stresses on the converter. Such shapes could be trapezoidal or sinusoidal in nature.

System design can also be expanded to encompass a larger operating space. It is presumed that the system response should be fairly linear as long as the machine is not in magnetic saturation, and therefore the ripple in the electrical and mechanical power waveforms will remain

low. Outside the operating envelope, however, there will be distortions due to the nonlinearities in the system that should be characterized.

From the system control standpoint, many avenues are open to exploration. For this work, a simple, open-loop voltage-vs-position controller was utilized for driving the machine phase. A more sophisticated approach would be to utilize a phase current controller with the voltage-vs-position included as a feed-forward term. As could be seen from the experimental results, there are deviations from a constant current in the experimental system. Similar behavior could be expected from other non-modeled operating regions, such as the magnetic saturation region described in the preceding paragraph, where the system does not match the assumed model. In such cases there may be a trade-off between maintaining low electrical power ripple or low mechanical power ripple. Criteria will have to be developed in order to arrive at an "optimal" excitation strategy for operating points and system parameters that deviate from the modeled system and its design point.

6.4 Conclusion

There are several fundamental contributions to the design and implementation of Doubly-Salient Reluctance Machines presented herein that eliminate two of the basic, presumed disadvantages of this type of machine: a large ripple in the electrical power, which required the use of electrolytic capacitor bank, and a large ripple in the mechanical power, which was embodied by a large torque ripple and precluded these machines for many applications. The development of the Shaped Reluctance Machine and DC Reluctance Machine allow for the design of machines with low or no ripple in their power waveforms and is a significant step forward in bringing these low-cost, robust machines into the market.

6.5 Publications

- N. S. Lobo, E. Swint, and R. Krishnan, "M-Phase N-Segment Flux-Reversal-Free Stator Switched Reluctance Machines," in *Industry Applications Society Annual Meeting, 2008. IAS '08. IEEE*, 2008, pp. 1–8.
- E. Swint and R. Krishnan, "Two-Phase SR Drive with Flux-Reversal Free Stator and Balanced Normal Forces," in *Industry Applications Society Annual Meeting, 2008. IAS '08. IEEE*, 2008, pp. 1–6.
- E. Swint and J. Lai, "Switched reluctance motor without torque ripple or electrolytic capacitors," in *2011 IEEE Energy Conversion Congress and Exposition (ECCE)*, 2011, pp. 1657–1663.
- E. Swint and J. Lai, "Shaped Reluctance Machine," Prepared for submission to *IEEE Transactions on Magnetics*.
- E. Swint and J. Lai, "DCRM: Reluctance Motor Drive System without Torque or Current Ripple" Submitted to *IEEE Transactions on Industry Applications* 13 January 2012.

References

[1] S. A. Nasar, "D.C.-switched reluctance motor," *Proceedings of the Institution of Electrical Engineers*, vol. 116, no. 6, pp. 1048-1049, Jun. 1969.

[2] P. J. Lawrenson, J. M. Stephenson, N. N. Fulton, P. T. Blenkinsop, and J. Corda, "Variable-speed switched reluctance motors," *Electric Power Applications, IEE Proceedings B*, vol. 127, no. 4, pp. 253-265, Jul. 1980.

[3] C. H. Lee, "Vernier Motor and Its Design," *IEEE Transactions on Power Apparatus and Systems*, vol. 82, no. 66, pp. 343-349, Jun. 1963.

[4] S. Sprague, *Lamination Steels*, 2nd ed. The Electric Motor Education and Research Foundation, 2002.

[5] G. Dunlop, "A switched-reluctance motor drive with zero torque ripple and a constant inverter bus current," *ARCHIVE: Proceedings of the Institution of Mechanical Engineers, Part I: Journal of Systems and Control Engineering 1991-1996 (vols 205-210)*, vol. 208, no. 19, pp. 61-68, Jun. 1994.

[6] J. Song-Manguelle, S. Schröder, T. Geyer, G. Ekemb, and J.-M. Nyobe-Yome, "Prediction of Mechanical Shaft Failures Due to Pulsating Torques of Variable-Frequency Drives," *IEEE Transactions on Industry Applications*, vol. 46, no. 5, pp. 1979-1988, Oct. 2010.

[7] B. Fahimi, G. Suresh, K. M. Rahman, and M. Ehsani, "Mitigation of acoustic noise and vibration in switched reluctance motor drive using neural network based current profiling," in *The 1998 IEEE Industry Applications Conference, 1998. Thirty-Third IAS Annual Meeting*, 1998, vol. 1, pp. 715-722 vol.1.

[8] R. Arumugam, J. F. Lindsay, and R. Krishnan, "Sensitivity of pole arc/pole pitch ratio on switched reluctance motor performance," in *Industry Applications Society Annual Meeting, 1988., Conference Record of the 1988 IEEE*, 1988, pp. 50-54 vol.1.

[9] J. P. Johnson, A. V. Rajarathnam, H. A. Toliyat, S. Gopalakrishnan, and B. Fahimi, "Torque optimization for a SRM using winding function theory with a gap-dividing surface," in *Industry Applications Conference, 1996. Thirty-First IAS Annual Meeting, IAS '96., Conference Record of the 1996 IEEE*, 1996, vol. 2, pp. 753-760 vol.2.

[10] N. K. Sheth and K. R. Rajagopal, "Optimum pole arcs for a switched reluctance motor for higher torque with reduced ripple," *Magnetics, IEEE Transactions on DOI - 10.1109/TMAG.2003.816151*, vol. 39, no. 5, pp. 3214-3216, 2003.

[11] D. P. Tormey and D. A. Torrey, "A comprehensive design procedure for low torque-ripple variable-reluctance motor drives," in *, Conference Record of the 1991 IEEE Industry Applications Society Annual Meeting, 1991*, 1991, pp. 244-251 vol.1.

[12] M. Moallem, C.-M. Ong, and L. E. Unnewehr, "Effect of rotor profiles on the torque of a switched-reluctance motor," *IEEE Transactions on Industry Applications*, vol. 28, no. 2, pp. 364-369, Apr. 1992.

[13] H. C. Lovatt and J. M. Stephenson, "Influence of number of poles per phase in switched reluctance motors," *Electric Power Applications, IEE Proceedings B*, vol. 139, no. 4, pp. 307-314, Jul. 1992.

[14] M. N. Anwar, I. Husain, and A. V. Radun, "A comprehensive design methodology for switched reluctance machines," *IEEE Transactions on Industry Applications*, vol. 37, no. 6, pp. 1684-1692, Dec. 2001.

[15] W. Pengov, J. R. Hendershot, and T. J. . Miller, “A new low-noise two-phase switched reluctance motor,” in *2005 IEEE International Conference on Electric Machines and Drives*, 2005, pp. 1281-1284.

[16] Seok-Gyu Oh and R. Krishnan, “Two-Phase SRM With Flux-Reversal-Free Stator: Concept, Analysis, Design, and Experimental Verification,” *IEEE Transactions on Industry Applications*, vol. 43, no. 5, pp. 1247-1257, Oct. 2007.

[17] K. F. Konecny, “United States Patent: 4647802 - Variable reluctance motor with reduced torque ripple,” U.S. Patent 464780203-Mar-1987.

[18] C. Neagoe, A. Foggia, and R. Krishnan, “Impact of pole tapering on the electromagnetic torque of the switched reluctance motor,” in *Electric Machines and Drives Conference Record, 1997. IEEE International*, 1997, p. WA1/2.1-WA1/2.3.

[19] S. F. Kolomeitsev and K. F. Brodsky, “United States Patent: 5844346 - Low torque ripple switched reluctance motor,” U.S. Patent 584434601-Dec-1998.

[20] Jung-Pyo Hong, Kyung-Ho Ha, and Ju Lee, “Stator pole and yoke design for vibration reduction of switched reluctance motor,” *Magnetics, IEEE Transactions on DOI - 10.1109/20.996239*, vol. 38, no. 2, pp. 929-932, 2002.

[21] N. Bhiwapurkar, A. K. Jain, and N. Mohan, “Study of new stator pole geometry for improvement of SRM torque profile,” in *Electric Machines and Drives, 2005 IEEE International Conference on*, 2005, pp. 516-520.

[22] Y Ozoglu and N. Guzelbyoglu, “EFFECT OF STATOR AND ROTOR POLE SHAPES ON THE TORQUE RIPPLE IN A SWITCHED RELUCTANCE MOTOR,” *Eleco Conference*, 1999.

[23] Y. Kano, T. Kosaka, and N. Matsui, "Optimum Design Approach for a Two-Phase Switched Reluctance Compressor Drive," *IEEE Transactions on Industry Applications*, vol. 46, no. 3, pp. 955-964, Jun. 2010.

[24] N. K. Sheth and K. R. Rajagopal, "Torque profiles of a switched reluctance motor having special pole face shapes and asymmetric stator poles," *Magnetics, IEEE Transactions on DOI - 10.1109/TMAG.2004.829841*, vol. 40, no. 4, pp. 2035-2037, 2004.

[25] M. Barnes, A. M. Michaelides, and C. Pollock, "The design and performance of a self-starting 2-phase switched reluctance drive," in *Power Electronics and Variable Speed Drives, 1996. Sixth International Conference on (Conf. Publ. No. 429)*, 1996, pp. 419- 423.

[26] Yong Kwon Choi, Hee Sung Yoon, and Chang Seop Koh, "Pole-Shape Optimization of a Switched-Reluctance Motor for Torque Ripple Reduction," *Magnetics, IEEE Transactions on DOI - 10.1109/TMAG.2006.892292*, vol. 43, no. 4, pp. 1797-1800, 2007.

[27] M. L. McClelland, "United States Patent: 6093993 - Set of laminations for a switched reluctance machine," U.S. Patent 609399325-Jul-2000.

[28] Jin Woo Lee, Hong Seok Kim, Byung Il Kwon, and Byung Taek Kim, "New rotor shape design for minimum torque ripple of SRM using FEM," *Magnetics, IEEE Transactions on DOI - 10.1109/TMAG.2004.824803*, vol. 40, no. 2, pp. 754-757, 2004.

[29] K. Ramu and N. S. Lobo, "United States Patent: 7015615 - Apparatus and method that prevent flux reversal in the stator back material of a two-phase SRM (TPSRM)," U.S. Patent 701561521-Mar-2006.

[30] P. Lawrenson, "United States Patent: 3448310," U.S. Patent 344831003-Jun-1969.

[31] J. Byrne and J. C. Lacy, "United States Patent: 3956678 - Electrodynamic system comprising a variable reluctance machine," U.S. Patent 395667811-May-1976.

[32] H. Torkaman, E. Afjei, and M. S. Toulabi, "New Double-Layer-per-Phase Isolated Switched Reluctance Motor: Concept, Numerical Analysis, and Experimental Confirmation," *IEEE Transactions on Industrial Electronics*, vol. 59, no. 2, pp. 830-838, Feb. 2012.

[33] A. C. Koenig and S. D. Pekarek, "Measurement of torque ripple in mass-produced switched-reluctance motor drives," in *2005 IEEE International Conference on Electric Machines and Drives*, 2005, p. 6 pp.-509.

[34] A. C. Koenig and S. D. Pekarek, "Feedback-Based Mitigation of Torque Harmonics in Switched Reluctance Motor Drives," in *APEC 2007 - Twenty Second Annual IEEE Applied Power Electronics Conference*, 2007, pp. 383-389.

[35] D. G. Taylor, M. Ilic'-Spong, R. Marino, and S. Peresada, "A feedback linearizing control for direct-drive robots with switched reluctance motors," in *1986 25th IEEE Conference on Decision and Control*, 1986, vol. 25, pp. 388-396.

[36] M. Ilic'-Spong, R. Marino, S. Peresada, and D. Taylor, "Feedback linearizing control of switched reluctance motors," *IEEE Transactions on Automatic Control*, vol. 32, no. 5, pp. 371- 379, May 1987.

[37] H. Le-Huy, R. Perret, and R. Feuillet, "Minimization of Torque Ripple in Brushless DC Motor Drives," *IEEE Transactions on Industry Applications*, vol. IA?22, no. 4, pp. 748-755, Jul. 1986.

[38] Y. Murai, Y. Kawase, K. Ohashi, K. Nagatake, and K. Okuyama, "Torque ripple improvement for brushless DC miniature motors," *IEEE Transactions on Industry Applications*, vol. 25, no. 3, pp. 441-450, Jun. 1989.

[39] R. S. Wallace and D. G. Taylor, "A balanced commutator for three-phase switched reluctance motors to minimize torque ripple," in *Systems Engineering, 1990., IEEE International Conference on*, 1990, pp. 597-600.

[40] R. S. Wallace and D. G. Taylor, "Torque Ripple Reduction in Three-Phase Switched Reluctance Motors," in *American Control Conference, 1990*, 1990, pp. 1526-1527.

[41] R. S. Wallace and D. G. Taylor, "Low-torque-ripple switched reluctance motors for direct-drive robotics," *Robotics and Automation, IEEE Transactions on*, vol. 7, no. 6, pp. 733-742, 1991.

[42] Han-Kyung Bae and R. Krishnan, "A novel approach to control of switched reluctance motors considering mutual inductance," in *26th Annual Confjerence of the IEEE Industrial Electronics Society, 2000. IECON 2000*, 2000, vol. 1, pp. 369-374 vol.1.

[43] L. B. Amor, O. Akhrif, L. A. Dessaint, and G. Olivier, "Adaptive Nonlinear Torque Control of a Switched Reluctance Motor," in *American Control Conference, 1993*, 1993, pp. 2831-2836.

[44] R. C. Kavanagh, J. M. . Murphy, and M. G. Egan, "Torque ripple minimization in switched reluctance drives using self-learning techniques," in *, 1991 International Conference on Industrial Electronics, Control and Instrumentation, 1991. Proceedings. IECON '91*, 1991, pp. 289-294 vol.1.

[45] D. S. Reay, M. Mirkazemi-Moud, T. C. Green, and B. W. William, “Fuzzy adaptive systems applied to the control of a switched reluctance motor,” in *, Proceedings of the 1994 IEEE International Symposium on Intelligent Control, 1994*, 1994, pp. 81-86.

[46] S. Mir, M. E. Elbuluk, and I. Husain, “Torque-ripple minimization in switched reluctance motors using adaptive fuzzy control,” *Industry Applications, IEEE Transactions on DOI - 10.1109/28.753642*, vol. 35, no. 2, pp. 461-468, 1999.

[47] Zhengyu Lin, D. S. Reay, B. W. Williams, and Xiangning He, “Torque Ripple Reduction in Switched Reluctance Motor Drives Using B-Spline Neural Networks,” *IEEE Transactions on Industry Applications*, vol. 42, no. 6, pp. 1445-1453, Dec. 2006.

[48] Yan Cai and Chao Gao, “Nonlinear Modeling of Switched Reluctance Motor Based on BP Neural Network,” in *Third International Conference on Natural Computation, 2007. ICNC 2007*, 2007, vol. 1, pp. 232-236.

[49] S. A. Bortoff, R. R. Kohan, and R. Milman, “Adaptive control of variable reluctance motors: a spline function approach,” *IEEE Transactions on Industrial Electronics*, vol. 45, no. 3, pp. 433-444, Jun. 1998.

[50] I. Agirman, A. M. Stankovic, G. Tadmor, and H. Lev-Ari, “Adaptive torque-ripple minimization in switched reluctance motors,” *IEEE Transactions on Industrial Electronics*, vol. 48, no. 3, pp. 664-672, Jun. 2001.

[51] P. L. Chapman and S. D. Sudhoff, “Design and precise realization of optimized current waveforms for an 8/6 switched reluctance drive,” *IEEE Transactions on Power Electronics*, vol. 17, no. 1, pp. 76-83, Jan. 2002.

[52] A. C. Koenig, S. D. Pekarek, and P. Lamm, "A PI-based control strategy for mitigation of torque harmonics in switched reluctance motor drives," in *Twenty-Third Annual IEEE Applied Power Electronics Conference and Exposition, 2008. APEC 2008*, 2008, pp. 363-369.

[53] I. Husain, "Minimization of torque ripple in SRM drives," *IEEE Transactions on Industrial Electronics*, vol. 49, no. 1, pp. 28-39, Feb. 2002.

[54] Dong-Hee Lee, Jianing Liang, Zhen-Guo Lee, and Jin-Woo Ahn, "A Simple Nonlinear Logical Torque Sharing Function for Low-Torque Ripple SR Drive," *Industrial Electronics, IEEE Transactions on DOI - 10.1109/TIE.2009.2024661*, vol. 56, no. 8, pp. 3021-3028, 2009.

[55] J. Y. Le Chenadec, B. Multon, and S. Hassine, "Current feeding of switched reluctance motor: Optimization of the current wave form to minimize the torque ripple," in *Proc. IMACS-TC1 4th Int. Conf.*, 1993, pp. pp. 267–272.

[56] V. P. Vujičić, "Minimization of Torque Ripple and Copper Losses in Switched Reluctance Drive," *IEEE Transactions on Power Electronics*, vol. 27, no. 1, pp. 388-399, Jan. 2012.

[57] H. J. Brauer, M. D. Hennen, and R. W. De Doncker, "Control for Polyphase Switched Reluctance Machines to Minimize Torque Ripple and Decrease Ohmic Machine Losses," *IEEE Transactions on Power Electronics*, vol. 27, no. 1, pp. 370-378, Jan. 2012.

[58] H. C. Lovatt and J. M. Stephenson, "Computer-optimised smooth-torque current waveforms for switched-reluctance motors," *Electric Power Applications, IEE Proceedings -*, vol. 144, no. 5, pp. 310-316, Sep. 1997.

[59] A. D. Cheok and Y. Fukuda, "A new torque and flux control method for switched reluctance motor drives," *IEEE Transactions on Power Electronics*, vol. 17, no. 4, pp. 543-557, Jul. 2002.

[60] R. B. Inderka and R. W. A. A. De Doncker, "DITC-direct instantaneous torque control of switched reluctance drives," *Industry Applications, IEEE Transactions on DOI - 10.1109/TIA.2003.814578*, vol. 39, no. 4, pp. 1046-1051, 2003.

[61] G. Vakil, P. Upadhyay, N. Sheth, A. Patel, A. Tiwari, and D. Miller, "Torque ripple reduction in the flux reversal motor by rotor pole shaping and stator excitation," in *Electrical Machines and Systems, 2008. ICEMS 2008. International Conference on*, 2008, pp. 2980-2985.

[62] R. M. Davis, W. F. Ray, and R. J. Blake, "Inverter drive for switched reluctance motor: circuits and component ratings," *Electric Power Applications, IEE Proceedings B*, vol. 128, no. 2, pp. 126-136, 1981.

[63] C. R. Neuhaus, N. H. Fuengwarodsakul, and R. W. De Doncker, "Control Scheme for Switched Reluctance Drives With Minimized DC-Link Capacitance," *Power Electronics, IEEE Transactions on*, vol. 23, no. 5, pp. 2557-2564, 2008.

[64] C. R. Neuhaus and R. W. De Doncker, "DC-link voltage control for Switched Reluctance Drives with reduced DC-link capacitance," in *Energy Conversion Congress and Exposition (ECCE), 2010 IEEE*, 2010, pp. 4192-4198.

[65] W. Suppharangsan and J. Wang, "A new switching technique for DC-link capacitor minimisation in switched reluctance machine drives," in *Power Electronics, Machines and Drives (PEMD 2010), 5th IET International Conference on*, 2010, pp. 1-6.

[66] E. Swint and J. Lai, “Switched reluctance motor without torque ripple or electrolytic capacitors,” in *2011 IEEE Energy Conversion Congress and Exposition (ECCE)*, 2011, pp. 1657-1663.